



Three Dimensional Localization of Lesions
from Digitized Mammograms

THESIS
Amy L. Magnus
Captain, USAF

AFIT/GEO/ENG/95D-04

DISTRIBUTION STATEMENT A

Approved for public release
Distribution Unlimited

DEPARTMENT OF THE AIR FORCE
AIR UNIVERSITY
AIR FORCE INSTITUTE OF TECHNOLOGY

Wright-Patterson Air Force Base, Ohio

DTIC QUALITY INSPECTED 1

AFIT/GEO/ENG/95D-04

Three Dimensional Localization of Lesions
from Digitized Mammograms

THESIS
Amy L. Magnus
Captain, USAF

AFIT/GEO/ENG/95D-04

Approved for public release; distribution unlimited

19960617 002

REPORT DOCUMENTATION PAGE			Form Approved OMB No. 0704-0188	
Public reporting burden for this collection of information is estimated to average 1 hour per response, including the time for reviewing instructions, searching existing data sources, gathering and maintaining the data needed, and completing and reviewing the collection of information. Send comments regarding this burden estimate or any other aspect of this collection of information, including suggestions for reducing this burden, to Washington Headquarters Services, Directorate for Information Operations and Reports, 1215 Jefferson Davis Highway, Suite 1204, Arlington, VA 22202-4302, and to the Office of Management and Budget, Paperwork Reduction Project (0704-0188), Washington, DC 20503.				
1. AGENCY USE ONLY (Leave blank)		2. REPORT DATE December 1995		3. REPORT TYPE AND DATES COVERED Master's Thesis
4. TITLE AND SUBTITLE Three Dimensional Localization of Lesions from Digitized Mammograms			5. FUNDING NUMBERS	
6. AUTHOR(S) Amy L. Magnus Captain, USAF				
7. PERFORMING ORGANIZATION NAME(S) AND ADDRESS(ES) Air Force Institute of Technology, WPAFB OH 45433-6583			8. PERFORMING ORGANIZATION REPORT NUMBER AFIT/GEO/ENG/95D-04	
9. SPONSORING / MONITORING AGENCY NAME(S) AND ADDRESS(ES) NA			10. SPONSORING / MONITORING AGENCY REPORT NUMBER	
11. SUPPLEMENTARY NOTES				
12a. DISTRIBUTION / AVAILABILITY STATEMENT Approved for public release; Distribution Unlimited			12b. DISTRIBUTION CODE	
13. ABSTRACT. (Maximum 200 words) This thesis describes new algorithms to localize regions-of-interests (ROIs) three dimensionally from a pair of digitized mammograms. This work is intended to add a layer of sophistication to computer aided diagnosis by putting to use the fixed and measurable parameters of mammographic imaging. The fixed parameters are the source to film orientation and the podium-image distance. Measurable parameters are the rotation angle of the x-ray tube from the horizontal and the compression depth (the distance from compression paddle to contact podium distance) at the time of imaging. As an additional benefit, three dimensional localization algorithms alleviate the confusion radiologists may have in determining the particular quadrant of a breast lesion identified for further examinations or biopsies. This feasibility investigation located microcalcifications within 10-15 mm and eliminates quadrant ambiguities. Accuracy measures are based on knowing the fixed parameters, source-image distance and podium-image distance, of the mammography imaging system with accuracies of ± 5 mm and ± 2 mm respectively and the adjustable parameters, x-ray tube rotation angle and the compression depth with accuracies of $\pm 5^\circ$ and ± 10 mm respectively.				
14. SUBJECT TERMS Breast Cancer, Pattern Recognition, Breast Cancer Detection, Breast Cancer Localization			15. NUMBER OF PAGES 66	
			16. PRICE CODE	
17. SECURITY CLASSIFICATION OF REPORT UNCLASSIFIED	18. SECURITY CLASSIFICATION OF THIS PAGE UNCLASSIFIED	19. SECURITY CLASSIFICATION OF ABSTRACT UNCLASSIFIED	20. LIMITATION OF ABSTRACT UL	

AFIT/GEO/ENG/95D-04

Three Dimensional Localization of Lesions
from Digitized Mammograms

THESIS

Presented to the Faculty of the Graduate School of Engineering
of the Air Force Institute of Technology

Air University

In Partial Fulfillment of the
Requirements for the Degree of
Master of Science in Electro-Optical Engineering

Amy L. Magnus, BSEE

Captain, USAF

December, 1995

Approved for public release; distribution unlimited

Acknowledgements

I would like to offer my sincerest thanks to my advisor, Dr Steven K. Rogers, for his insight and enthusiasm. Thank you also to my committee members, Major Jeff Hoffmeister and Capt Rick Raines, for their contributions. In his experience, with his expertise, Major Jeff Hoffmeister is an invaluable resource to the Breast Cancer Detection Group and greatly enriched this effort. I thank Susan Poteat of the Wright-Patterson AFB Hospital for teaching me the mechanics of mammography. Kudos to the faculty members of the Engineering and the Mathematics Departments, especially LtCol Martin Styzx and Capt Michael Stoecker, for their help in developing the algorithms herein.

I consider myself incredibly fortunate to work with such peers as those in the Breast Cancer Detection Group – Capt William Polakowski, Capt Ronald Dauk, and Lt Dru McCandless. Special thanks to Dave Bramlag who spent many extra hours tailoring the image database for me.

Thank you, Linda, for being a sounding board... and for loaning me your laptop. To Laura, Antony, Jesse, and Chris... thank you for keeping me in play.

To Sandra McCoy-Cleveland – my mother, friend and fellow masters student – my gratitude for the love and support you set my way. It was all dearly felt. Praises to all my family for giving me a strong base.

Amy L. Magnus

Table of Contents

	Page
Acknowledgements	ii
List of Figures	vi
Abstract	viii
 I. Introduction	 1-1
1.1 Statement of the Problem	1-4
1.2 Scope	1-4
1.3 Overview	1-5
 II. Background	 2-1
2.1 State of the Art in Mammography	2-1
2.1.1 Advances in Equipment	2-1
2.1.2 Motivations for Breast Compression	2-1
2.1.3 Rotating X-ray Tube	2-2
2.1.4 Summary	2-4
2.2 Standard Views	2-4
2.2.1 Optimal Positioning	2-4
2.2.2 Medial Lateral Oblique View	2-5
2.2.3 Craniocaudal View	2-5
2.2.4 MLO and CC as Complementary Views	2-7
2.2.5 Summary	2-7
 III. Compression Model	 3-1
3.1 The Uncompressed Breast as an Ellipsoid of Revolution	3-1
3.1.1 Terminology	3-1

	Page
3.1.2 Volume	3-1
3.2 Study of Compressed Objects	3-2
3.2.1 Object Selection Criteria	3-2
3.2.2 Notation	3-3
3.2.3 Compression Effects	3-3
3.3 Development of Compression Recovery Parameters	3-7
3.3.1 Uniform Compression	3-7
3.3.2 Compression to a Uniform Thickness	3-8
3.3.3 Compression Recovery Parameters	3-14
3.4 Summary	3-15
IV. Mammography Imaging	4-1
4.1 Point Source Geometry	4-1
4.1.1 Projection of an Object Point	4-1
4.1.2 Projection of a Compressed Object Point	4-3
4.1.3 Recovery of Entire Line-of-Sight to Object Curve	4-4
4.1.4 Magnification/Minification	4-5
4.2 Determining Compression Depth	4-5
4.3 Compression Recovery Parameters, Final Form	4-6
4.4 3D Localization	4-8
4.4.1 Alignment and Reconstruction of Symmetric Breast	4-8
4.4.2 3D Localization	4-15
4.4.3 Cross Projection	4-18
4.5 Summary	4-19
V. Implementaion	5-1
5.1 Algorithm Implementation	5-1
5.1.1 Front End Processing	5-1

	Page
5.1.2 Indexing	5-3
5.2 Implementation Modelling	5-4
VI. Conclusions	6-1
Bibliography	BIB-1
Vita	VITA-1

List of Figures

Figure	Page
1.1. Illustration of radiologist's mammography review	1-2
2.1. Effects of breast compression on image quality	2-2
2.2. Dedicated mammography unit with rotating anode x-ray tube.	2-3
2.3. Anatomical references for radiographic views	2-5
2.4. MLO view by anatomical references	2-6
2.5. CC view by anatomical references	2-6
2.6. Standard mammograms of a right breast	2-8
2.7. Disproportionate aspects for the CC and MLO views	2-9
2.8. Desired aspects for CC and MLO Views	2-9
3.1. Half-ellipsoid of revolution	3-3
3.2. Imaging systems with different object-source ratios	3-5
3.3. Utilization of compression to effectively reduce object-source ratio . . .	3-6
3.4. Maximum extent of nipple line as projection of ellipsoid's pole	3-7
3.5. Notational references for breast ellipsoid	3-8
3.6. Cross section of flattened breast ellipsoid.	3-11
4.1. Front view of dedicated mammography unit	4-2
4.2. Line-of-sight in projection of an object point	4-2
4.3. Object curve	4-8
4.4. Input image convention	4-9
4.5. Initial single-image alignment for CC view	4-11
4.6. Initial single-image alignment for MLO view	4-11
4.7. Line-of-Sight in compressed space.	4-13
4.8. Orientation of MLO and CC views to the object horizontal	4-14

Figure	Page
4.9. Rendition of discrete MLO and CC object lines	4-15
4.10. Lesion localized in three dimensions	4-16
5.1. 3D Algorithm Implementation within CADx System	5-2
5.2. Modelled error dependency example	5-5

Abstract

This thesis describes new algorithms to localize regions-of-interests (ROIs) three dimensionally from a pair of digitized mammograms. This work is intended to add a layer of sophistication to computer aided diagnosis by putting to use the fixed and measurable parameters of mammographic imaging. The fixed parameters are the source to film orientation and the podium-image distance. Measurable parameters are the rotation angle of the x-ray tube from the horizontal and the compression depth (the distance from compression paddle to contact podium distance) at the time of imaging.

As an additional benefit, three dimensional localization algorithms alleviate the confusion radiologists may have in determining the particular quadrant of a breast lesion identified for further examinations or biopsies.

This feasibility investigation located microcalcifications within 10-15 *mm* and eliminates quadrant ambiguities. Accuracy measures are based on knowing the fixed parameters, source-image distance and podium-image distance, of the mammography imaging system with accuracies of ± 5 *mm* and ± 2 *mm* respectively and the adjustable parameters, x-ray tube rotation angle and the compression depth with accuracies of $\pm 5^\circ$ and ± 10 *mm* respectively.

Three Dimensional Localization of Lesions from Digitized Mammograms

I. Introduction

Cancer of the breast is one of the major health problems of women: it is our most common malignancy and second most deadly after lung cancer. The 5-year relative survival figures for breast cancer found in pre-invasive, invasive, or metastatic stages are, respectively, 92 percent, 71 percent, and 18 percent. [1] These statistics compiled by the National Cancer Institute imply that breast cancer in the metastatic stage - cancer that has spread to other parts of the body - is a much more serious disease... where, for many, detection and treatment have come too late. Therefore, the detection, prevention and control of breast cancer in its early stages are foremost in the minds of patients, medical personnel and researchers.

Mammography has proven the most valuable tool in breast cancer screening due to the radiologists' ability to detect early cancers with a high degree of sensitivity and a reasonable degree of specificity. In a 14-year study, the Breast Cancer Detection Demonstration Projects demonstrated the extent of mammography's utility. [2, 3] Of the cancers categorized as minimal (lesions less than 1 cm in diameter or pre-invasive), only 6 percent were detected during a physical examination by a professional using palpation. The remaining minimal cancers were either identified by mammography alone (57 percent) or by both mammography and physical examination (37 percent). With modern mammography equipment, the risk of radiation-induced cancers is so minute that annual mammography examinations are universally recommended to women ages 50 and above. Additional data suggests that women ages 40 to 49 would also benefit from the same annual examination [4, 3]; but, at present, prohibitive cost and the limited number of trained radiologists precludes the expanded use of mammography. [5, 6]

The process of reviewing mammograms may be made more efficient with the inclusion of an automated detection system. The radiologist would remain the primary reviewer

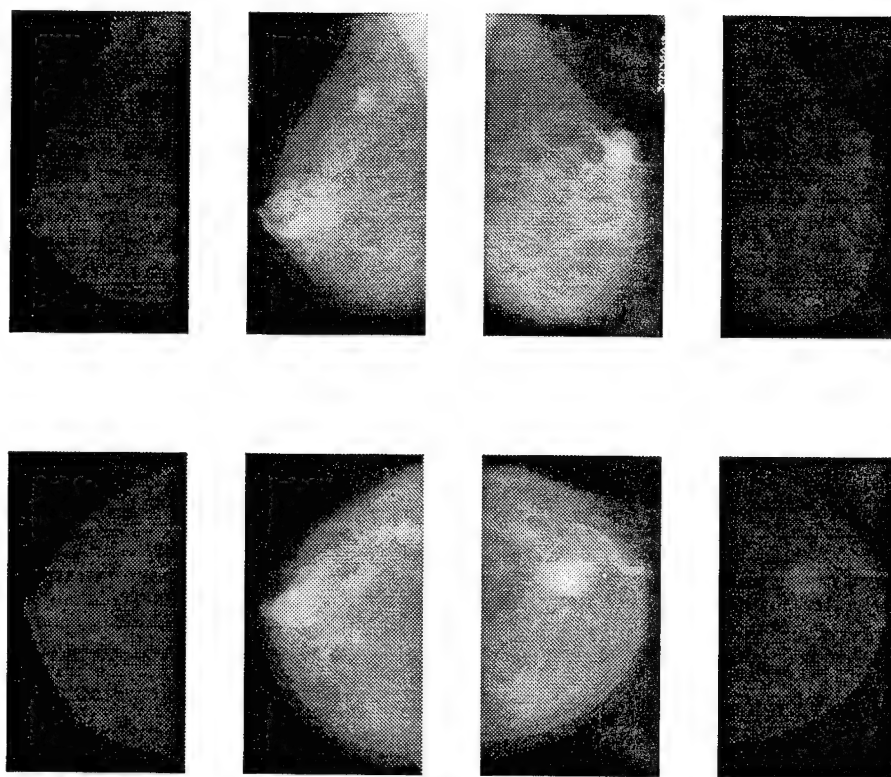


Figure 1.1 Illustration of typical mammography review. The center four images are from the patient's most recent screening; outside images represent the set from the patient's previous mammography examination. The four images on the right depict the patient's left breast; the left images correspond to the right breast. This arrangement matches the orientation of the patient facing the reviewer.

but delegate quality control responsibilities to a Computer Aided breast cancer Diagnosis (CADx) system which would provide a "second opinion" in diagnosis. [7]

To provide acceptable quality control, a CADx system must be on par with the radiologist – taking advantage of all the information the radiologist has available from the full mammography examination. The annual mammography examination is done in three parts: an interview of the patient where a history relative to breast disease is taken, a physical examination of the breasts in search of palpable lesions, and the actual mammography screening. The standard mammography screening consists of four images: that is, two images of each breast taken at different aspects, or views. Upon review by a radiologist, the films are arranged so that the corresponding views of the right and left breast appear as mirror images. This arrangement is illustrated in Fig. 1.1 which includes the placement

of films from the patient's last screening. The films are arranged to facilitate (1) the detection of asymmetries between the contralateral, or "mirrored", views, (2) three dimensional localization of asymmetries in the complementing views of the same breast, and (3) the evaluation of changes since the last screening. In addition to these cues, the radiologist may be prompted by a physician or by the patient themselves to concentrate attention in a specific region where a palpable lesion was detected or some other symptom that may point to malignancy. A clinically viable CADx system must be tuned to detect subtleties on the order of those apparent to a radiologist without generating false detections, or "false positives", that would unnecessarily distress the patient and care-givers.[5]

Predominately, the work in CADx systems [8, 9, 10, 11, 12, 13, 14] has concentrated on single-image strategies to recognize abnormalities in texture and other visual patterns. Additionally, several researchers [7, 15, 16, 17] have compared contralateral breast views – as the radiologist does – to detect asymmetries. The basic alignment techniques of these works follow:

- Yin, *et al*, align the mammography films of the right and left breast by hand prior to digitization. [7]
- Hand, *et al*, translate the contralateral breast views up and down, left and right to achieve the "best" fit. [16]
- Kimme, *et al*, account for variations in the size and shapes of the contralateral breast when they divide the breast into sections that will feed their segmentation module. [17]
- After translating and rotating the breast to align edge features, Lau, *et al*, remap all the pixels of the left breast area to the right breast area based on the width and height ratios of the breast boundaries. [15]

All of the above works relied on the assumption that the aspect angles are the same for the contralateral views.

No substantial work has been published on region-of-interest (ROI) verification through three dimensional localization of asymmetries or abnormalities. In 1979, Spiesberger sketched out a strategy for verifying the detection of a small lesion by comparing the

craniocaudal (CC) and lateral medial (LM) views of a breast. [18] Spiesberger presented no physical basis for his algorithm, and he did not go into any great detail about its implementation since it required the processing of entire mammograms which at the time was infeasible.

Three dimensional localization of lesions from mammograms is extremely difficult problem due to the many variances in mammography imaging... particularly those imposed by the use of breast compression. Nevertheless, the implementation of standardized practices in mammography has put three dimensional localization within reach.

The advances that have made this work possible are:

- The use of dedicated mammography equipment.
- The standardization of radiographic views and patient positioning procedures.
- The availability of computational resources that can handle high resolution images of entire mammograms.

1.1 Statement of the Problem

In the development of Computer Aided breast cancer Diagnosis (CADx) systems modeled after the radiologists' mammography review, the next logical step is to implement a three dimensional localization strategy that verifies the detection of malignant lesions from complementing mammography views. This thesis develops a compression recovery model and back-projection algorithms that achieve that end.

1.2 Scope

The 3D localization algorithms herein are developed specifically for standard mammography screenings where craniocaudal (CC) and medial lateral oblique (MLO) radiographic views are performed and where the mammography unit is equipped with a 90° compression paddle.

To support this work, mammogram films were obtained from the Wright-Patterson Air Force Base (WPAFB) Hospital. The films were digitized to 12 bits of grayscale at

a resolution of $100\mu\text{m}$. The digitized images were cropped to 2048×1024 pixels. The locations of film edges were preserved in a database.

The algorithms proposed are part of a CADx system that serves to re-cue the radiologist to potentially malignant areas in a set of mammograms. The algorithms were written in the Matlab software environment and augmented by C routines tailored to the application.

1.3 Overview

Chapter II presents the key advances in mammography imaging and the standardized patient-positioning procedures. Chapter III examines the effects of compression on the breast and develops the compression recovery models crucial to this work. Chapter IV incorporates the compression recovery models into the geometry imposed by the mammography imaging system. Chapter V charts the entire 3D localization algorithm and presents preliminary results. Chapter VI discusses the conclusions regarding the usefulness of this work.

II. Background

In the past two decades, the arrival of dedicated diagnostic tools and new medical procedures has led to an increase in detection of precancerous and non-invasive breast lesions. This chapter presents the state of the art in mammography and a more detailed discussion of its current practice. The material will underline the advancements that have made this work both possible and necessary.

2.1 State of the Art in Mammography

2.1.1 Advances in Equipment. High quality mammography employs dedicated machines known as film/screen x-ray units. An innovation developed in the early 1970's and in widespread use by the early 1980's, film/screen x-ray units employ lower radiation levels and shorter exposure times than the industrial non-film/screen x-ray units traditionally used for bone and chest x-rays. Film/screen x-ray units were designed to make annual mammography plausible by lowering the patient's exposure to radiation. Immediately, however, added benefits were realized. Though image resolution of film/screen is inherently less than that of industrial non-screen film, the lower radiation levels result in improved contrast, and the shorter exposure time reduces blurring due to movement – a significant problem in mammography since the breast is near the heart. Film/screen mammography has outdistanced industrial film in terms of overall image quality with new film technology, and additional innovations which include a fixed source to film orientation with longer source-to-image distance, smaller focal spots, and the use of breast compression. [5]

2.1.2 Motivations for Breast Compression. Vigorous compression is mandatory for acceptable image quality as it promotes: [5, 19]

- Improved resolution.
- Improved geometric sharpness by reducing the object to image receptor distance.
- Improved image contrast by decreasing breast thickness thus reducing radiation scattering.

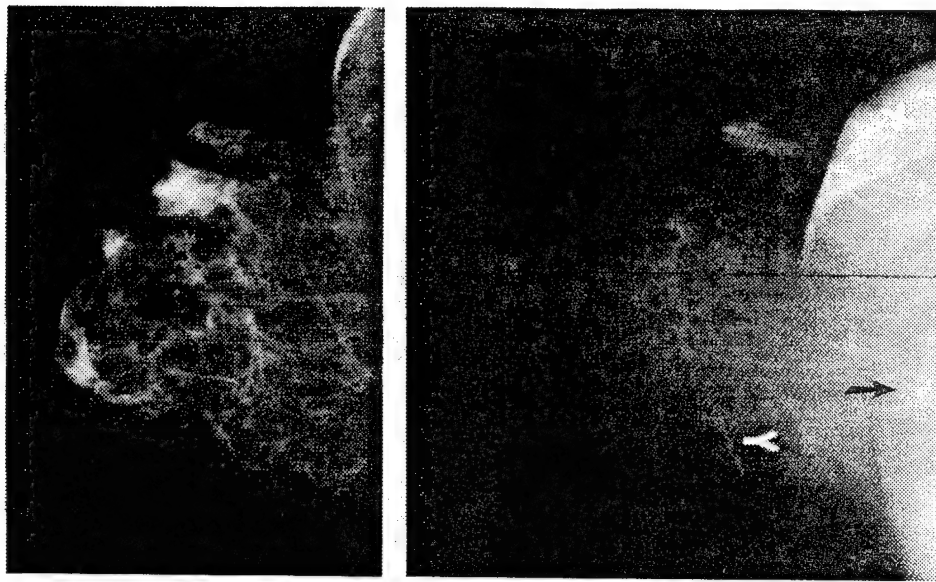


Figure 2.1 Effects of breast compression on image quality. The sharper mammogram on the left is the CC view of a compressed breast. The mammogram on the right was taken of the same breast, from the same aspect, but without compression. [19]

- Minimization of image blurring due to motion by preventing patient movement during exposure.
- Separation of breast structures which lessens the likelihood of the obscuration of a lesion.
- Uniform exposure of posterior and anterior parts of the breast by conforming breast to a uniform thickness.

Two mammograms are presented in Fig. 2.1 which depict the same breast compressed and uncompressed respectively. The image of the compressed breast is better for depicting tissue throughout the entire breast. The image of the uncompressed breast was used to view a lesion near the chest wall (marked by dark arrow) but has poor contrast in the anterior part of breast. The uncompressed breast image is blurred significantly by motion, and the breast boundary – the transition from breast tissue to background – is more subtle.

2.1.3 Rotating X-ray Tube. Another key innovation in modern mammography equipment has made the orientation of the patient to the x-ray tube easier. In an annual

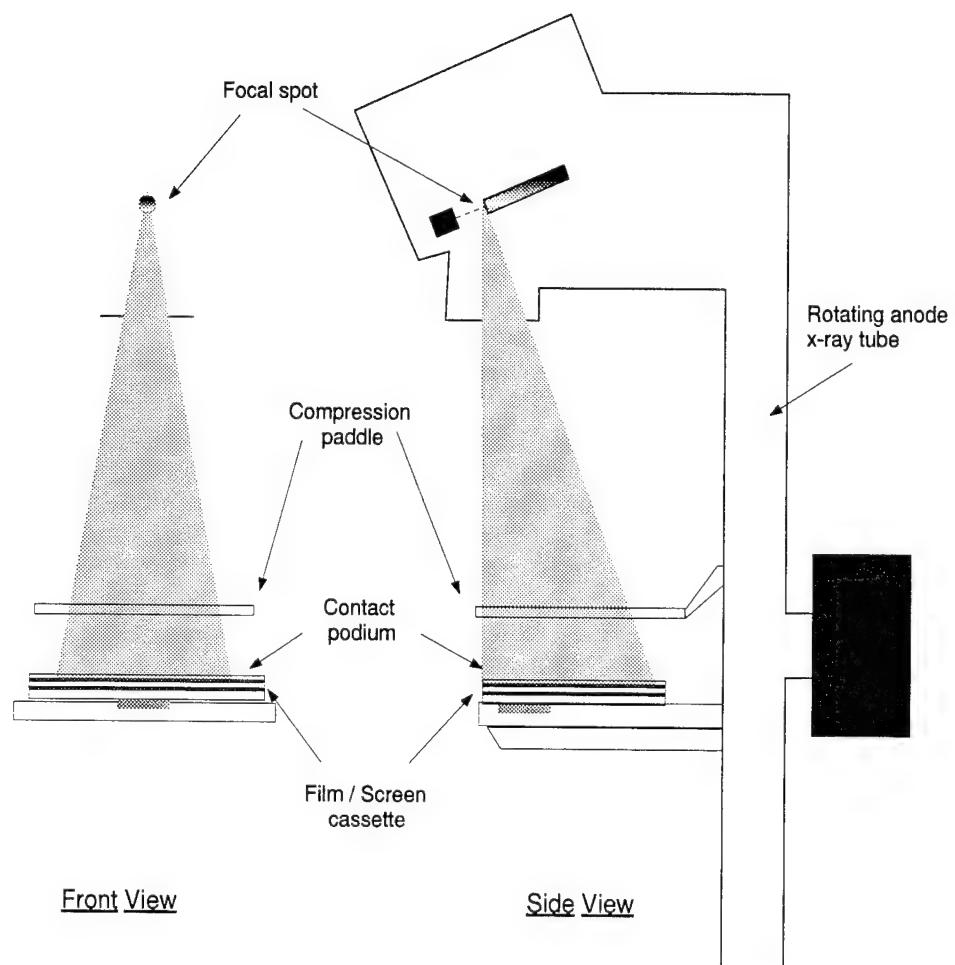


Figure 2.2 Dedicated mammography unit with rotating anode x-ray tube.

mammography screening, the patient stands and the x-ray tube rotates. Figure 2.2 provides a drawing of a mammography system with rotating anode x-ray tube. The versatility of this setup alleviates the need to move the patient into awkward positions and has allowed the standard use of viewing positions refined to the anatomy and mobility of the breast. These refined views and their advantages are discussed further in Section 2.2. [19, 20]

2.1.4 Summary. Of the innovations in modern mammography units, the fixed source-to-film position and small spot size facilitate 3D localization. Unfortunately, breast compression complicates the undertaking by scaling the dimensions in alternate views disproportionately.

Since vigorous compression is used to procure high quality mammograms, a compression recovery model must be developed.

2.2 Standard Views

The versatility of the rotating x-ray tube has led to the refinement of standard viewing positions which adapt to the anatomy and natural mobility of the breast. As a consequence, many medical facilities perform the medial lateral oblique and the craniocaudal views in all annual mammography screenings. Figure 2.3 illustrates anatomical references for the radiographic views: [19, 20]

These standardized views and their well-documented patient-positioning procedures work with the natural shape of the breast – minimizing potential distortions and maximizing the predictability of key “landmark” locations. These landmarks – which include the nipple line and the pectoral muscle wall – are required to enable proper alignment of the image view to its counterpart. [19, 21, 20]

2.2.1 Optimal Positioning. The optimal radiographic view depicts as much breast tissue as possible. Accordingly, as compression is applied normally to the image plane, care must be taken to avoid moving the compression paddle against the fixed tissues of the breast. The fixed aspects of the breast are the medial and superior margins; the mobile aspects are the lateral and the inferior margins. In an optimal view, the radiologic

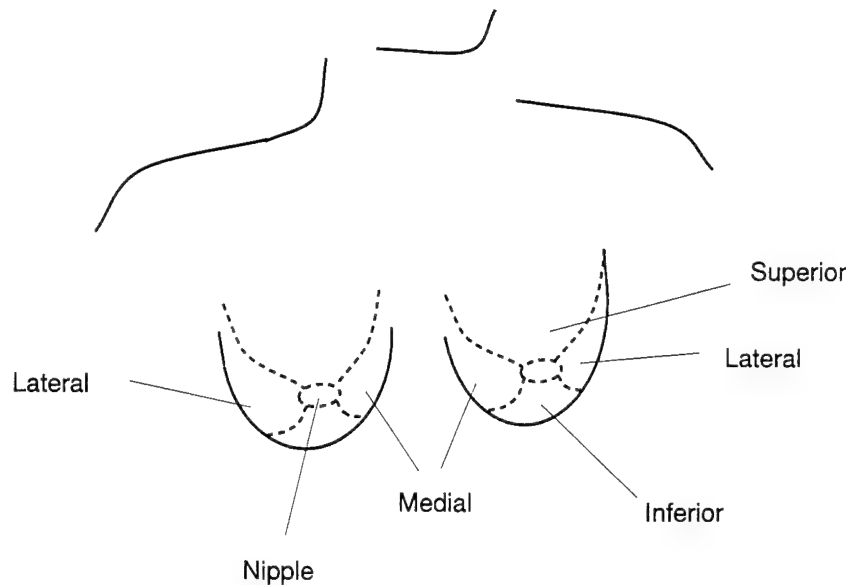


Figure 2.3 Anatomical references for radiographic views. [5]

technologist lifts the mobile tissue of the patient's breast away from the chest wall and towards the fixed tissue. [19, 20]

2.2.2 Medial Lateral Oblique View. The medial lateral oblique (MLO) view offers the best opportunity to image all of the breast tissue in a single mammogram, particularly the superolateral portion of the breast where most breast cancers are found. As shown in Fig. 2.4, the x-ray beam is directed from the superomedial to the inferolateral aspect of the breast. The image receptor is placed parallel to the patient's pectoral muscle, so that the image plane is at an angle of 30° to 60° from the horizontal. In an ideal MLO view as in Fig. 2.6, the pectoral muscle is visible, inframammary fold is open, and the nipple is in profile. Typically, the nipple line of the MLO view appears at an angle to the film axes. [19]

2.2.3 Craniocaudal View. The craniocaudal (CC) view augments the MLO view and captures the medial tissue that the latter view might have missed. As depicted in Fig. 2.5, the x-ray beam is directed from the superior portion of the breast to the inferior, or from "head-to-tail" as its name implies. The image receptor, and thus image plane, is parallel to the horizontal. Figure 2.6 contains a CC view mammogram. The pectoral

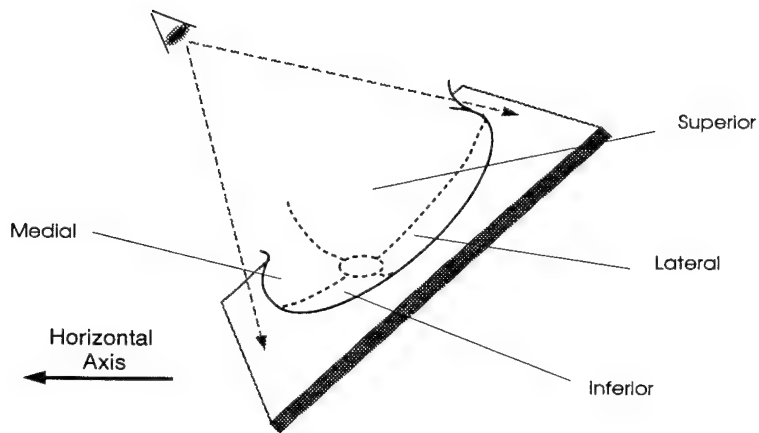


Figure 2.4 MLO view by anatomical references: Positioning for the medial lateral oblique view of the left breast.

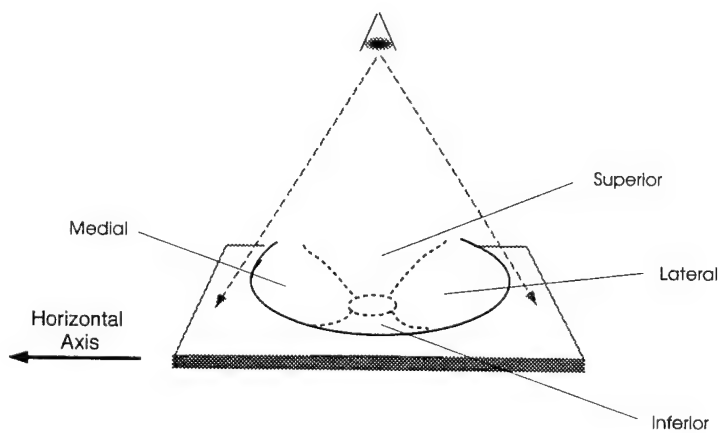


Figure 2.5 CC view by anatomical references: Position for the craniocaudal view of the left breast.

muscle is visible in only 20 % of all CC views. Ideally, the nipple is centered, and the nipple line of the CC view is nearly aligned with the film axes. [19]

2.2.4 MLO and CC as Complementary Views. The nipple line is a projection of the shared axis of the MLO and CC view. If the angular difference of x-ray tube between the views is known and the angular difference of the nipple line on the films is determined, the only imaging parameters that stand in the way of triangulation is the degree of object distortion imposed by breast compression.

Due to compression, the breast's dimensions are seen disproportionately by each view as illustrated in Fig. 2.7. If one attempted to back-project from a point-of-interest to its respective source, the resulting lines-of-sight for the MLO and CC views would not intersect meaningfully except where the object-of-interest lies along the rotation axis. (The rotation axis is coming out of the page and depicted at the nipple in Fig. 2.7.) If the compressed breast can be rescaled properly as in Fig. 2.8, it becomes possible to back-project from corresponding points-of-interest to their respective sources and to localize an object-of-interest in three dimensional space at the intersection of the scaled lines-of-sight.

2.2.5 Summary. The use of dedicated mammography units and the standardization of patient positioning have made the products of mammography more predictable. However, the effects of breast compression must be understood and reversed for 3D localization schemes to work.

The next chapter presents a compression model applicable to mammography and develops expressions for compression recovery parameters.

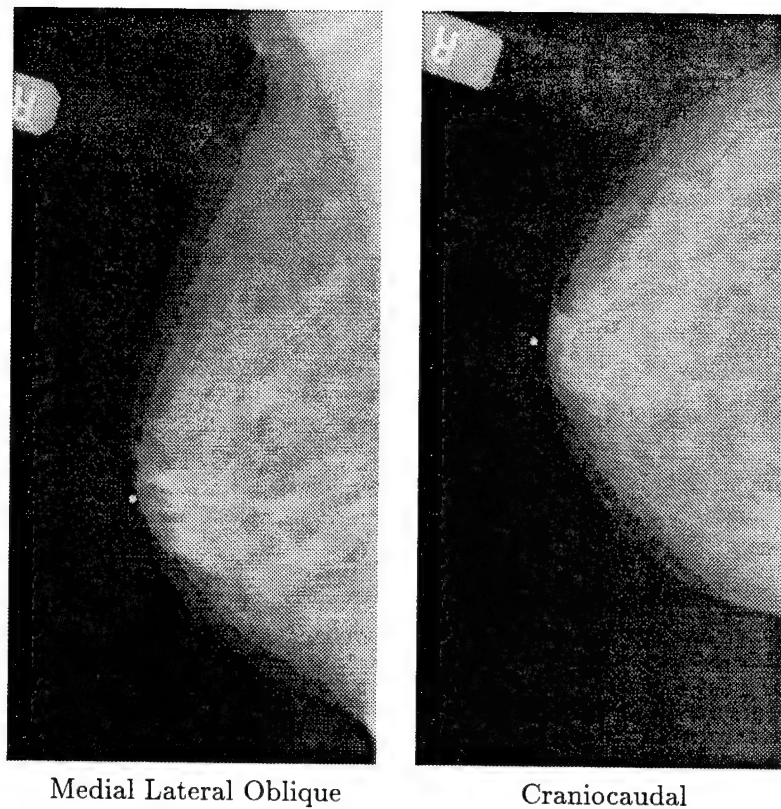


Figure 2.6 Standard mammograms of a right breast. Note, in both views, the nipple is in profile and is marked by a 2mm lead BB. For the MLO view, the pectoral muscle wall clearly visible in the upper right-hand corner, and in the lower right-hand corner, the inframammary fold is open.

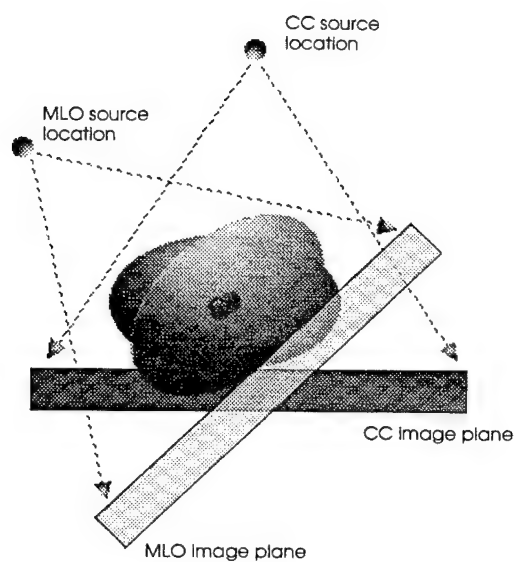


Figure 2.7 Disproportionate aspects of a left breast for the CC and MLO views due to breast compression.

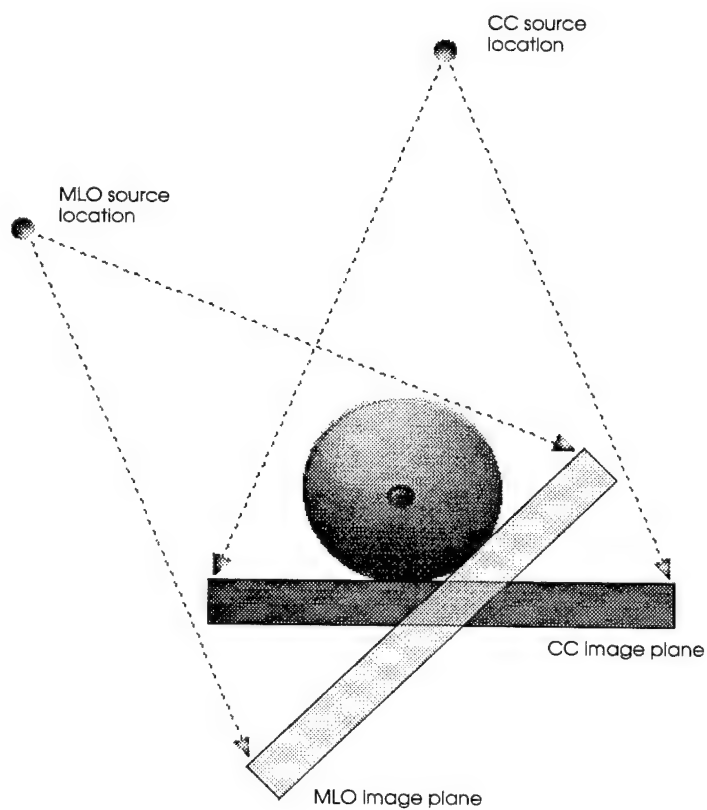


Figure 2.8 Desired aspects of left breast for CC and MLO Views.

III. Compression Model

The goal of compression recovery is to reconform the breast to a basic shape which the computer, the radiologist and the physician can readily interpret. This chapter will present a model for the breast's shape, the conclusions from an empirical study of compression effects on similar objects, and the development of expressions for compression recovery parameters.

3.1 The Uncompressed Breast as an Ellipsoid of Revolution

The shape of the uncompressed breast can be modeled as a half ellipsoid of revolution. This is the generic shape to which a breast would conform if its tissue could support its own weight.

3.1.1 Terminology. An ellipsoid of revolution, as seen in Fig. 3.1, is defined as the ellipsoid generated by revolving an ellipse about one of its axes. Sections in planes perpendicular to the fixed axis are all circles. [22]

The fixed axis is designated the axis of revolution. In mammography, patient positioning ensures that the axis of revolution is parallel to the image plane. This axis is a key reference: it is about the axis of revolution that the object is compressed, decompressed and rotated between MLO and CC views. As an added convention, the "aspect plane" will refer to the plane that contains the axis of revolution and runs parallel to the image plane. The intersection of the MLO aspect plane and the CC aspect plane is the axis of revolution. The pole of the half-ellipsoid is the intersection of the half-ellipsoid and the axis of revolution. [22]

The semiaxes of the half-ellipsoid are established as a , b and c : where $a = c \neq b$ as seen in Fig. 3.1. [22]

3.1.2 Volume. The volume of a half-ellipsoid is: $Volume = \frac{2}{3}\pi abc$. When compression is applied to the breast, we will assume that volume is preserved. If the half-ellipsoid experiences uniform compression normal to the axis of revolution, then [22]:

$$Volume = \frac{2}{3}\pi abc = \frac{2}{3}\pi a'b'c' \quad (3.1)$$

where the c semiaxis is compressed by a factor C so that:

$$c' = c/C \quad (3.2)$$

$$a'b' = Cab \quad (3.3)$$

If the breast's physical structure allowed it to expand equally in all directions normal to the force of compression, then $a' = \sqrt{C}a$ and $b' = \sqrt{C}b$. However, in studying fibrous objects, it becomes obvious that the physical nature of breast tissue prominently favors expansion in one direction. The next section will detail the observations made in applying vigorous compression to breast-like objects.

3.2 Study of Compressed Objects

Breast compression is accomplished by pressing the tissue between a 90° compression paddle and a contact podium which contains the x-ray film. This arrangement is depicted in Fig. 3.5. Under vigorous compression, the breast experiences 25 to 35 pounds of force. The degree of compression is determined by the pliancy of the tissue and the amount of discomfort the patient can tolerate during the screening procedure. According to quality control guidelines, vigorous compression must be applied so that, at a minimum, the breast tissue is taut and gentle tapping does not indent the skin. At maximum, the compression should be less than painful. [19, 23]

3.2.1 Object Selection Criteria. To understand the effects of compression, natural-occurring objects have been studied under vigorous compression. The chosen objects are composed of soft, fibrous tissue surrounded by a layer of skin. Their shapes - though variable - suggest ellipsoids whose semiaxes a , b and c meet the criteria $a \approx c < b$ where the major semiaxis, b , runs along the grain of the fibrous tissue. The objects' criteria

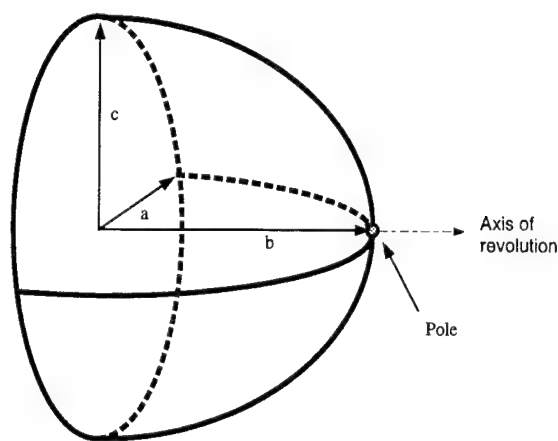


Figure 3.1 Half-ellipsoid of revolution ($a = c \neq b$). Axis of revolution is along \hat{y} axis

match the physical nature of the breast. The “grain” of the breast is provided by the network of ducts and fibrous connective tissue that extend from the nipple and to mammary lobules. In other words, the grain of the breast and the axis of revolution run parallel to the nipple line.

3.2.2 Notation. To clarify a test object’s orientation, reference axes are assigned as follows:

- The \hat{y} axis is the axis of revolution.
- The \hat{z} axis is parallel to the force of compression and thus normal to the image plane.
- The \hat{x} axis is perpendicular to \hat{y} and \hat{z} .

Note that that the orientation of the \hat{x} and \hat{z} axes is dependent on the viewing aspect of the breast. The \hat{y} axis is the only reference axis common to the MLO and CC views.

3.2.3 Compression Effects.

3.2.3.1 Unequal Deformation of Axes. When vigorous compression is applied along the \hat{z} axis of a test object, the object expands along \hat{x} , or along the dimension perpendicular the object’s grain. In each case, the object changed only subtly along its \hat{y} axis. This reaction is due to the fibrous nature of the tissue which resists expansion

along the grain. The compressed object – which adapts to conserve volume – adjusts in the dimension in which it is most free to move.

If uniform compression is applied to the ellipsoid as described in Section 3.1.1, the object reacts according to Eqs. 3.1 through 3.3. From the physical nature of fibrous tissue, its dimensions along the \hat{y} axis will remain unchanged, and so:

Given the geometric conditions,

$$\begin{aligned} Volume &= \frac{2}{3}\pi abc = \frac{2}{3}\pi a'b'c' \\ a &= c \end{aligned}$$

and given the compression conditions,

$$\begin{aligned} c' &= c/C \\ b' &= b \end{aligned}$$

it follows:

$$\begin{aligned} a' &= C \cdot a \\ a' &= C^2 \cdot c' \end{aligned} \tag{3.4}$$

Therefore, if c' and a' are known the compression factor can be calculated:

$$C = \sqrt{\frac{a'}{c'}} \tag{3.5}$$

and the original object's dimensions recovered:

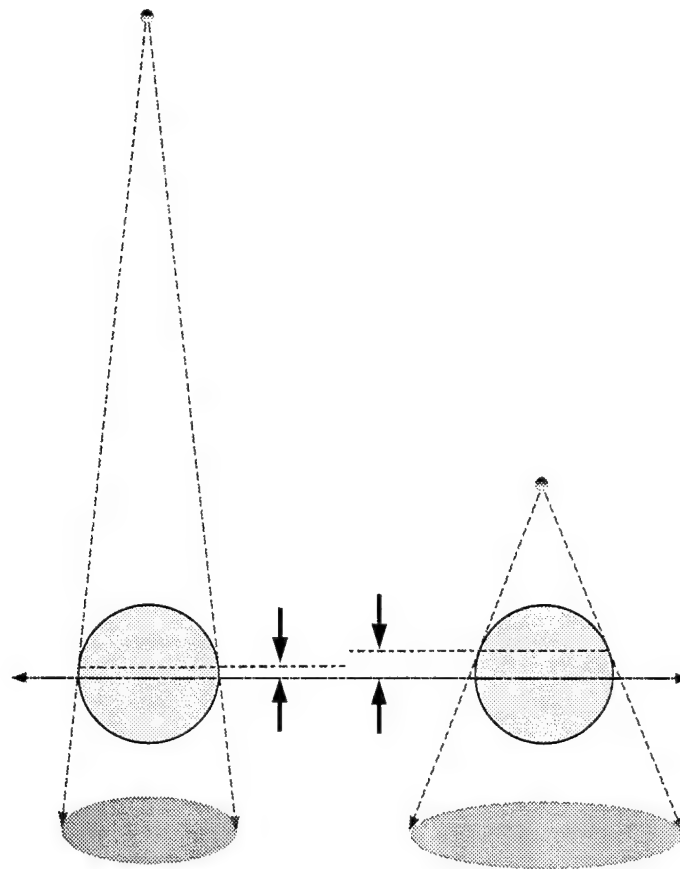


Figure 3.2 Comparison of two imaging systems with different object-source ratios. Note that the imaging system with the larger source-image distance projects its shadow from a plane closer to its aspect plane (solid axis) than the imaging system with a smaller source-image distance.

$$a = \frac{a'}{C} \quad (3.6)$$

$$c = C \cdot c' \quad (3.7)$$

$$a = \sqrt{a'c'} = c \quad (3.8)$$

3.2.3.2 Location of Aspect Plane. Soft tissue under vigorous compression will distribute its volume symmetrically between the compression paddle and podium so that the thickest cross section of the object lies in a plane half way between the paddle and podium. This plane is denoted as the aspect plane. If the object is illuminated by a far

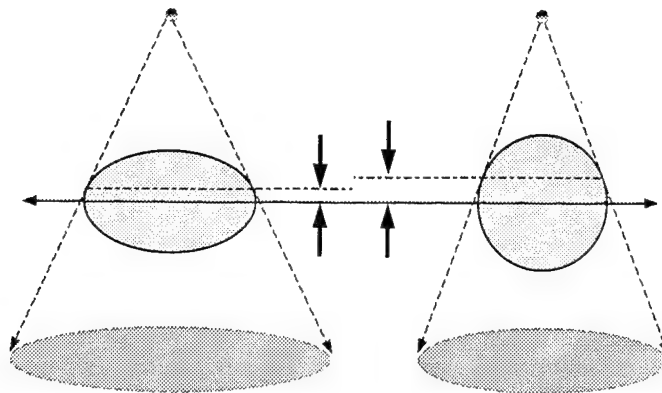


Figure 3.3 Utilization of compression to effectively reduce object-source ratio. The compressed object projects its shadow closer to its aspect plane (solid axis) than the uncompressed object.

field source, the object will cast a shadow defined by its cross section in the aspect plane. A far field source has a low object-source ratio – a ratio given by the object distance to the image plane over the source distance to the image plane. The shadows cast by imaging systems of different object-source ratios are illustrated in Fig. 3.2.

Object compression lowers the object-source ratio of the imaging system (see Fig. 3.3), giving the advantages of a far field source without the disadvantages. Specifically, the geometric sharpness of the image improves without excessive attenuation of the x-ray field since the field travels through a thinner layer of absorbing/scattering tissue.

3.2.3.3 Point of Common Reference on Axis of Revolution. A common reference point must be found to align the aspect planes of the MLO and CC views. Recall that the ellipsoidal object experiences no expansion or contraction along its \hat{y} axis regardless of compression applied or the rotation of \hat{z} about \hat{y} . Again, if the compressed object is illuminated by a far field source as in Fig. 3.4, the maximum extent of its shadow in the \hat{y} direction will be projected from a predictable physical point. This predictable physical point corresponds to the pole of the half-ellipsoid.

On both the MLO or CC mammogram, the pole of the ellipsoidal breast is projected to an image point denoted y_{max} as it is the maximum extent of the breast boundary in \hat{y} direction. The location of the pole will be established as the origin of the reference axes in both the MLO and CC view.

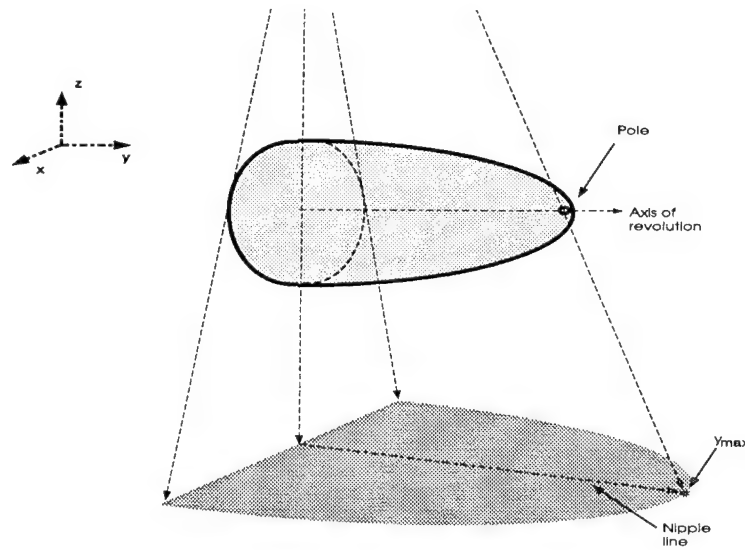


Figure 3.4 Maximum extent of nipple line corresponds to pole of the half-ellipsoid. The nipple line is the projection of axis of revolution onto the image plane.

3.3 Development of Compression Recovery Parameters

3.3.1 Uniform Compression. A general recovery scheme can be developed using Eqs 3.5-3.7 and applied to any point $\mathcal{O}_c = [x_c, y_c, z_c]^T$ within the compressed ellipsoid. Assuming the origin $[0, 0, 0]^T$ is at the center of the original ellipsoid, the point $\mathcal{O} = [x_o, y_o, z_o]^T$ corresponds to \mathcal{O}_c where:

$$C = \sqrt{\frac{a'}{c'}}$$

$$x_o = \frac{x_c}{C}$$

$$y_o = y_c$$

$$z_o = C \cdot z_c$$

The above calculations can be done using one simple matrix transformation:

$$\mathcal{O} = \mathbf{S} \mathcal{O}_c \tag{3.9}$$

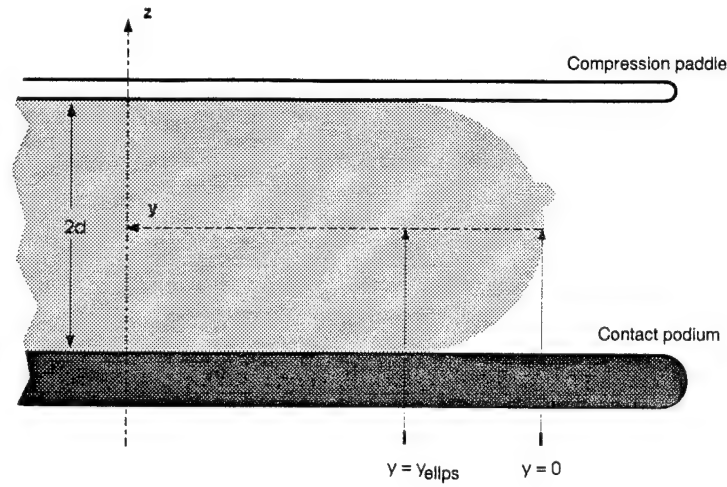


Figure 3.5 Notational references for breast ellipsoid. The \hat{x} axis is out of the page.

where \mathbf{S} is expressed by compression recovery parameters, γ_x and γ_z :

$$\gamma_x = \sqrt{\frac{c'}{a'}} \quad (3.10)$$

$$\gamma_z = \sqrt{\frac{a'}{c'}} \quad (3.11)$$

$$\mathbf{S} = \begin{bmatrix} \gamma_x & 0 & 0 \\ 0 & 1 & 0 \\ 0 & 0 & \gamma_z \end{bmatrix} \quad (3.12)$$

Since \mathbf{S} is a diagonal matrix, its inverse is easily determined and can be used to model the compression of an object point:

$$\mathcal{O}_c = \mathbf{S}^{-1} \mathcal{O} \quad (3.13)$$

3.3.2 Compression to a Uniform Thickness. If the compression paddle exerted a uniform compression on the breast ellipsoid, the compression recovery parameters could be found by Eqs. 3.10 and 3.11. However, reality is more complicated. The 90° compression paddle does not exert uniform compression, but compresses the anterior to posterior

parts of the breast to a uniform thickness. The resulting deformed shape of the breast is a flattened ellipsoid. The tip of the breast has an elliptical cross section in the \hat{x} - \hat{z} plane and, thus, experiences uniform compression. However, in the posterior region of the breast beginning at a certain distance y_{ells} from the pole, the skin collapses against the compression plate, and the \hat{x} - \hat{z} cross section takes the generic form of Fig. 3.6. The cross section can be approximated by a box flanked by two half ellipses.

The anterior tip of the compressed breast ellipsoid experiences uniform compression. Only one calculation is necessary to compute γ_x and $\frac{1}{\gamma_z}$ in this region. The posterior region of the breast experiences compression to a uniform depth. The compression recovery parameters are not constant in this region and do not have a reciprocal relationship. Equations 3.10-3.12 are generalized to:

$$\gamma_x(y) = \frac{r(y)}{d} \quad (3.14)$$

$$\gamma_z(y) = \frac{r(y)}{w(y)/2} \quad (3.15)$$

$$\mathbf{S}(y) = \begin{bmatrix} \gamma_x(y) & 0 & 0 \\ 0 & 1 & 0 \\ 0 & 0 & \gamma_z(y) \end{bmatrix} \quad (3.16)$$

where

- The uncompressed object radius, $r(y)$, is the radius of the \hat{x} - \hat{z} cross section from the original ellipsoid of revolution.
- The compression depth, $2d$, is the distance between the compression paddle and the contact podium, and d is the distance between the aspect plane and the podium.
- The compressed object width, $w(y)$, is the x dimensional width of the \hat{x} - \hat{z} cross section.

Equations 3.14-3.16 can implement the uniform compression model and the uniform thickness model in the anterior and posterior region of the breast respectively if the following conventions are used:

$$w(y) = \begin{cases} w(y_{ellps}) & : 0 \leq y \leq y_{ellps} & : \text{uniform compression model} \\ w(y) & : y_{ellps} \leq y < y_{center} & : \text{uniform thickness model} \end{cases} \quad (3.17)$$

$$r(y) = \begin{cases} r(y_{ellps}) & : 0 \leq y \leq y_{ellps} & : \text{uniform compression model} \\ r(y) & : y_{ellps} \leq y < y_{center} & : \text{uniform thickness model} \end{cases} \quad (3.18)$$

Before proceeding further, it should be noted that the parameters $\gamma_x(y)$ and $\gamma_z(y)$ are approximations of $\gamma_x(x, y)$ and $\gamma_z(x, y)$; this is easily seen as linear scaling will not return the flattened elliptical cross section of the compressed breast to a circular cross section. However, as y and $l(y)$ increase, the line-of-sight that extends from an image point on the mammogram to the source point approaches the normal \hat{z} so that variations in x along this line are small.

3.3.2.1 Determining the Uncompressed Object Radius, $r(y)$. Recall that the \hat{y} axis is unaffected by compression. Therefore, one can equate the volume of a thin slice from the original breast ellipsoid to the volume of the comparable slice from the compressed ellipsoid. The differential slice from the original ellipsoid is a cylinder of height Δy and radius $r(y)$ where $y_{ellps} \leq y \leq y_{center}$. The differential slice from the flattened ellipsoid is a flattened cylinder of height Δy and the cross section given in Fig. 3.6. Since the heights of the slices are the same, the areas of their cross sections can be equated:

$$\frac{Volume(slice)}{\Delta y} = \pi \cdot r(y)^2 = 2d \cdot l(y) + \pi \cdot d \cdot \frac{w(y) - l(y)}{2} \quad (3.19)$$

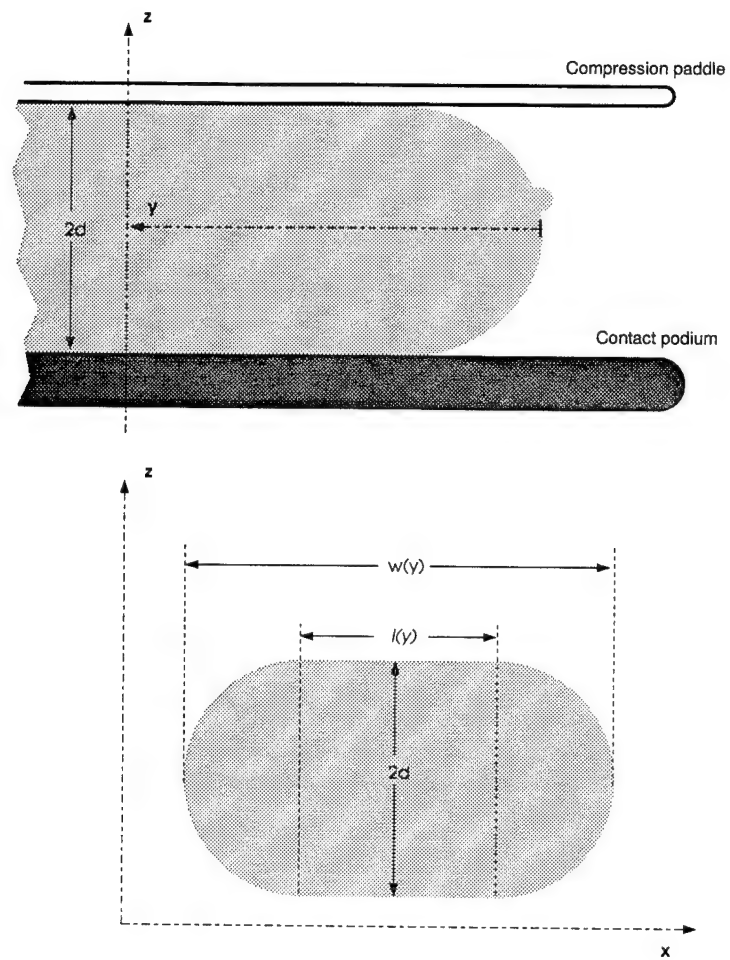


Figure 3.6 Cross section of flattened breast ellipsoid.

Solving for r :

$$r(y) = \sqrt{d \cdot \frac{w(y) - l(y)}{2} + \frac{2d \cdot l(y)}{\pi}} \quad (3.20)$$

$$= \sqrt{\frac{d \cdot w(y)}{2}} \cdot \sqrt{1 + \frac{l(y)}{w(y)} \left(\frac{4}{\pi} - 1 \right)} \quad (3.21)$$

Since $l(y) < w(y)$, $\frac{l(y)}{w(y)} \left(\frac{4}{\pi} - 1 \right)$ is less than 1. Using the Taylor expansion, where $\sqrt{1 + small} \simeq 1 + \frac{small}{2}$, $r(y)$ can be approximated:

$$r(y) \simeq \sqrt{\frac{d \cdot w(y)}{2}} \cdot \left[1 + \frac{1}{2} \cdot \frac{l(y)}{w(y)} \left(\frac{4}{\pi} - 1 \right) \right] \quad (3.22)$$

The constant $\frac{1}{2} \cdot \left(\frac{4}{\pi} - 1 \right) \cong 0.137$. If $r(y)$ is approximated using an elliptical cross section,

$$r_{approx}(y) = \sqrt{\frac{d \cdot w(y)}{2}} \quad (3.23)$$

then this assumption yields a 7% error if $l(y) = w(y)/2$. From the empirical object study, $l(y) = w(y)/2$ is a likely condition. An error of this size is untenable this early in the calculation of the compression recovery parameters, so we are motivated to depart from a pure elliptical model and develop estimates for y_{ellps} and $l(y)$.

3.3.2.2 Estimation of y_{ellps} . Recall that y_{ellps} is the distance from the pole of the breast ellipsoid to the y location where the skin collapses against the compression paddle. Revisiting the empirical object study discussed in Section 3.2, we have considered an object's cross section in the $x = 0$ plane denoted as $\mathcal{X}(0, y, z)$. The cross section $\mathcal{X}(0, y, z)$, depicted in Fig. 3.5, contains the axis of revolution and the \hat{z} axis. When soft-tissue objects are placed under vigorous compression, the anterior tip of $\mathcal{X}(0, y, z)$ is consistently circular as is the medial and lateral tips of the $\mathcal{X}(x, y_{center}, z)$, the object's cross section in the $y = y_{center}$ plane.

The forces that cause this phenomenon are the same forces that conform a fluid-filled bubble to a sphere [24]. The bubble is minimizing its surface tension given the pressure

exerted by its internal fluids. A soft-tissue object would react similarly if gravity, friction or structural forces are negligible compared to the pressures of the object's fluid. Under vigorous compression, the skin of the breast remains in contact with the compression paddle until the surface of least tension can pull the skin away from the compression paddle and transition to a resting posture against the podium. In the limit of high compression, the anterior tip of $\mathcal{X}(0, y, z)$ is a complete half circle with d as the radius of the circle. Recall that $2d$ is the distance between the compression paddle and contact podium and that d is the height of the aspect plane above the contact podium as depicted in Fig. 3.5. As in Fig. 3.5, if the pole of the breast ellipsoid defines the location of $y = 0$, then

$$y_{ellps} = d \quad (3.24)$$

3.3.2.3 Estimation of $l(y)$. The \hat{x} - \hat{z} cross section of the flattened ellipsoid (illustrated in Fig. 3.6) is estimated as a box flanked by two half-ellipses. The parameter $l(y)$ is the x dimension of the box. From the observations of the $\mathcal{X}(0, y, z)$ and $\mathcal{X}(x, y_{center}, z)$ cross sections in compressed objects (see Section 3.3.2.2), the only locations where $l(y)$ is known are $0 \leq y \leq y_{ellps}$ and $y = y_{center}$ where respectively $l(y) = 0$ and $l(y_{center}) = w(y_{center}) - 2 y_{ellps}$. Using Eq. 3.24 and Eq. 3.4, where $a' = w(y_{ellps})$ and $c' = d$, we compare the dimension $w(y) - l(y)$ at two locations: (1) $y = y_{ellps} = d$ and (2) $y = y_{center}$.

$$\begin{aligned} w(y_{ellps}) - l(y_{ellps}) &= w(y_{ellps}) = 2 C^2 d \\ w(y_{center}) - l(y_{center}) &= 2 y_{ellps} = 2 d \end{aligned}$$

Since the compression factor C is always greater than 1, $w(y_{ellps}) - l(y_{ellps})$ is always greater than $w(y_{center}) - l(y_{center})$. In fact, from the empirical object study, the dimension $w(y) - l(y)$ is in general near a maximum at $y = y_{ellps}$. A minimum estimate of $l(y)$ is determined by subtracting $w(y_{ellps})$ from $w(y)$. Taking in account all possible y locations,

$$l_{est}(y) = \begin{cases} 0 & : 0 \leq y \leq d \\ w(y) - w(d) & : d \leq y < y_{center} \end{cases} \quad (3.25)$$

3.3.3 Compression Recovery Parameters. The calculation of the compression recovery parameters will incorporate the two compression models: uniform compression and compression to a uniform thickness. By inserting Eqs. 3.17, 3.18, 3.24 and Eq. 3.25 into Eq. 3.20, the uncompressed object radius, $r(y)$, takes the form:

$$r(y) = \begin{cases} \sqrt{d \cdot \frac{w(d)}{2}} & : 0 \leq y \leq d \\ \sqrt{d \cdot \frac{w(d)}{2} + \frac{2d \cdot [w(y) - w(d)]}{\pi}} & : d \leq y \leq y_{center} \end{cases} \quad (3.26)$$

Compression recovery parameters are obtained from the generalized expressions, Eqs. 3.14-3.17 and the above expression for $r(y)$, Eq. 3.26:

$$\gamma_x(y) = \begin{cases} \sqrt{\frac{2d}{w(d)}} & : 0 \leq y \leq d \\ \frac{r(y)}{w(y)/2} & : d \leq y \leq y_{center} \end{cases} \quad (3.27)$$

$$\gamma_z(y) = \begin{cases} \sqrt{\frac{w(d)}{2d}} & : 0 \leq y \leq d \\ \frac{r(y)}{d} & : d \leq y \leq y_{center} \end{cases} \quad (3.28)$$

$$\mathbf{S}(y) = \begin{bmatrix} \gamma_x(y) & 0 & 0 \\ 0 & 1 & 0 \\ 0 & 0 & \gamma_z(y) \end{bmatrix} \quad (3.29)$$

where the application of $\mathbf{S}(y)$ depends on the y component of the compressed object point.

Since the scaling function does not transform the y component of a three dimensional point, the y component of the compressed object point and the uncompressed object point are the same. Thus, the inverse of $\mathbf{S}(y)$ can be used to model compression without modification:

$$\mathbf{S}^{-1}(y) = \begin{bmatrix} \frac{1}{\gamma_z(y)} & 0 & 0 \\ 0 & 1 & 0 \\ 0 & 0 & \frac{1}{\gamma_z(y)} \end{bmatrix} \quad (3.30)$$

3.4 Summary

In this chapter, expressions for the compression recovery parameters have been developed so that their calculation requires knowledge of d and $w(y)$ as seen in Fig 3.6 and as discussed below:

The compressed object width, $w(y)$, can be found from the breast boundary, or “skin” edge, on the mammogram. The breast boundary is a projection of the breast’s cross section in the aspect plane. Since the small source spot of a mammography unit yields a diverging beam (see Fig. 2.2), the projected cross section width, $w_p(y_p)$, is a magnified version $w(y)$. (See the shadows cast in Figs. 3.2 and 3.3.) Section 4.3 will develop the final expressions for the compression recovery parameters $\gamma_z(y)$ and $\gamma_z(y)$ in terms of w_p .

The compression paddle height, $2d$, is a condition of imaging that – under current practices – must be recorded by the radiologic technologist. If a fixed lead BB is placed at a known location on the compression plate and projected onto the film, d can also be determined from the mammogram. The implementation of this added practice is discussed in Section 4.2.

Now that the object variances have been addressed, we are poised to implement the 3D localization algorithms. All that remains to be considered is the imaging geometry of the mammography unit. These considerations and the 3D localization algorithms are presented in Chapter IV.

IV. Mammography Imaging

This chapter discusses the imaging geometry of a mammography unit and completes the development of compression recovery parameters. The final section of this chapter presents the 3D localization algorithms.

4.1 Point Source Geometry

The diverging x-ray beam of a mammography unit magnifies the image of an object based on the object's height above the image plane. As in Fig. 2.2, the x-ray beam of a mammography unit is produced by bombarding a small metal target with an electron beam. The target area is typically 0.3-0.4mm in diameter and tilted to direct the x-ray beam to the image receptor. The effective spot size of the source approximates a point source which produces a diverging beam. The magnification of an imaged object can be predicted by considering a line-of-sight that runs from the source through the object and onto the image plane. [25]

4.1.1 Projection of an Object Point. Consider the simplified imaging system given by Fig. 4.1 and 4.2. The source-image distance is given by SID , and the podium-image distance by pid . Selecting a cylindrical coordinate system where a point is given by $[radius \angle angle, z]$, the \hat{z} axis is set normal to the image plane. The image plane is located at $z = 0$; and, for now, pid is assumed to be zero. The point source Q located at $Q = [0, SID]$. An object point O located at an arbitrary location above the image plane so that $O = [r_o \angle \alpha, h]$. The line-of-sight is drawn from point Q through point O to image plane. The intersection of the line-of-sight and the image plane given by the projected point $P = [r_{proj} \angle \alpha, 0]$ where:

$$\begin{aligned} \frac{r_o}{r_{proj}} &= \frac{SID - h}{SID} \\ \text{or} \\ r_o &= r_{proj} \cdot \left(1 - \frac{h}{SID}\right) \end{aligned} \tag{4.1}$$

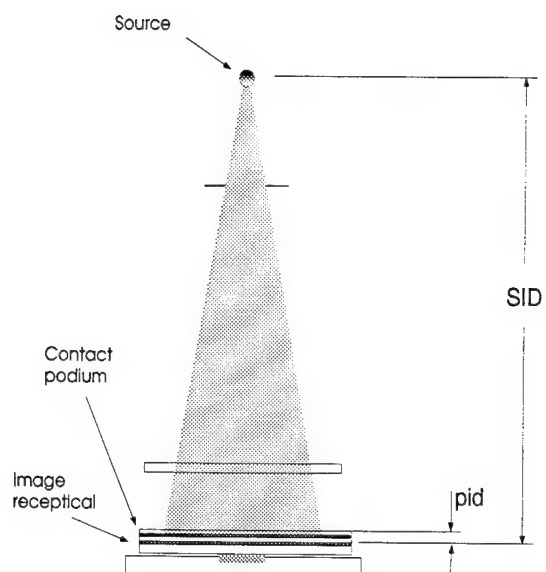


Figure 4.1 Detail of Fig. 2.2: Front view of dedicated mammography unit. The fixed source-image distance (SID) and podium-image distance (pid) are labeled.

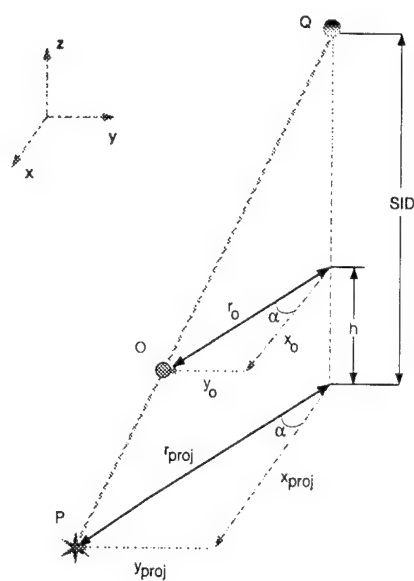


Figure 4.2 Projection of object point O from point source Q . Line-of-sight connects points Q, O, P

Having determined this simple relationship from similar triangles, we will now convert to Cartesian coordinates. This is the best notation since object compression will affect the x and y components of the radial distance r_o disproportionately. Points Q , \mathcal{O} , and P in Cartesian coordinates are given as column vectors of the form $[x, y, z]^T$ so that:

$$Q = \begin{bmatrix} 0 \\ 0 \\ SID \end{bmatrix}$$

$$\mathcal{O} = \begin{bmatrix} x_o \\ y_o \\ h \end{bmatrix}$$

$$P = \begin{bmatrix} x_{proj} \\ y_{proj} \\ 0 \end{bmatrix}$$

where from similar triangles:

$$x_o = x_{proj} \cdot \left(1 - \frac{h}{SID}\right) \quad (4.2)$$

$$y_o = y_{proj} \cdot \left(1 - \frac{h}{SID}\right) \quad (4.3)$$

$$x_{proj} = \frac{x_o}{1 - \frac{h}{SID}} \quad (4.4)$$

$$y_{proj} = \frac{y_o}{1 - \frac{h}{SID}} \quad (4.5)$$

4.1.2 Projection of a Compressed Object Point. The object is compressed using the fibrous tissue model discussed in Chapter III. The compressed object point is now $\mathcal{O}_c =$

$[C_x \cdot x_o, y_o, \frac{h}{C_z}]^T$. When the object point is illuminated by the source at $Q = [0, 0, SID]^T$, the projected point P_c is given by $[x_{c_p}, y_{c_p}, 0]^T$ where:

$$x_{c_p} = \frac{C_x \cdot x_o}{1 - \frac{h/C_z}{SID}} \quad (4.6)$$

$$y_{c_p} = \frac{y_o}{1 - \frac{h/C_z}{SID}} \quad (4.7)$$

Note that due to the denominators of Eqs. 4.6 and 4.7, x_{c_p} and y_{c_p} have a non-linear relationship with x_{proj} and y_{proj} . The non-linear term depends on the height of the original object. Since we generally do not know the height of the object above the image plane, this relationship is not optimal for our purposes. We would prefer to adjust the line-of-sight in compressed space to a line-of-sight that represents all possible locations of the uncompressed object from image plane to source point.

4.1.3 Recovery of Entire Line-of-Sight to Object Curve. If the uncompressed object point was illuminated by a source located at $Q_{effective} = [0, 0, C_z \cdot SID]^T$, x_{c_p} and y_{c_p} are linearly proportional to the x and y components of $P_{effective}$ projected point $[x_p, y_p, 0]^T$ where:

$$x_p = \frac{x_o}{1 - \frac{h}{C_z \cdot SID}} = \frac{x_{c_p}}{C_x} \quad (4.8)$$

$$y_p = \frac{y_o}{1 - \frac{h}{C_z \cdot SID}} = y_{c_p} \quad (4.9)$$

Essentially what we have done is adjust the entire line-of-sight in compressed space by weighting the \hat{x} and \hat{z} axis by $\frac{1}{C_x}$ and C_z respectively. In applying these weights denoted as compression recovery parameters, a new line-of-sight is constructed in uncompressed space. The new line-of-sight will hereafter be referred to as the object curve. The object curve represents all possible locations of the uncompressed object given points Q , P_c , the compression recovery parameters. No knowledge of the original object height is required to construct the object curve!

4.1.4 *Magnification/Minification.* Using the conventions outlined for Eqs. 4.6-4.9, a point – compressed or uncompressed – can be expressed in terms of its projection:

$$x = \frac{x_p}{M} = x_p \cdot m \quad (4.10)$$

$$y = \frac{y_p}{M} = y_p \cdot m \quad (4.11)$$

where M is the magnification of the projection and m is the minification of the back-projection defined as:

$$M = \frac{1}{1 - \frac{h/C_z}{SID}} \quad (4.12)$$

$$m = 1 - \frac{h/C_z}{SID} \quad (4.13)$$

The dimension $\frac{h}{C_z}$ is the distance from the compressed object point to the image plane. To simplify the above derivations, we assumed the podium-image distance, pid , was zero. In actual fact, we include pid in the $\frac{h}{C_z}$ term, so that, if the uncompressed object height is h_o , then

$$\frac{h}{C_z} = \frac{h_o}{C_z} + pid = \frac{h_o + C_z \cdot pid}{C_z} \quad (4.14)$$

The effective podium-image distance for the uncompressed object is then $pid_{effective} = C_z \cdot pid$. This effective distance is consistent with our strategy of applying compression recovery parameters along the entire length of the line-of-sight.

4.2 *Potential for Determining Compression Depth from Mammogram*

The object's compression depth, $2d$, is an important parameter required in the calculate the compression recovery parameters in Section 3.3.3. Due to the magnification of the diverging beam, it is possible to determine compression depth $2d$ if a lead BB is placed

on top of the compression paddle at a known location and imaged onto the mammogram. If the thickness of the compression paddle is given by pad and the BB-to-source point distance is represented by the vector $[x_{BB}, y_{BB}, SID - 2d - pid - pad]^T$, then, for example, y_{BB} can be expressed in terms of its corresponding projection dimension on the film y_{BB_p} :

$$y_{BB} = y_{BB_p} \cdot \left(1 - \frac{2d + pid + pad}{SID}\right) \quad (4.15)$$

Solving for the object compression depth $2d$:

$$2d = SID \cdot \left(1 - \frac{y_{BB}}{y_{BB_p}}\right) - pid - pad \quad (4.16)$$

The projected distance y_{BB_p} can be expressed in terms of y_{BB} and a difference term Δ such that $y_{BB_p} = y_{BB} + \Delta$. The equation for $2d$ simplifies to:

$$2d = \frac{SID \cdot \Delta}{y_{BB} + \Delta} - pid - pad \quad (4.17)$$

The uncertainty of $2d$ is strongly dependent on the resolution of image, the ratio of $SID \cdot \frac{y_{BB}}{(y_{BB} + \Delta)^2}$ (or simply $\frac{SID}{y_{BB}}$ when $\Delta \ll y_{BB}$) and the uncertainties of pid and pad .

4.3 Compression Recovery Parameters in Terms of the Projected Object Width, $w_p(y_p)$

This section finalizes the equations for the compression recovery parameters incorporating $w_p(y_p)$, the projection of the compressed object width, $w(y)$. Recall from Fig. 3.6 that $w(y)$ is an x dimension with a height d above the contact podium so that from Eqs. 4.10, 4.11, and 4.13:

$$m = 1 - \frac{d + pid}{SID} \quad (4.18)$$

$$w(y) = m \cdot w_p(y_p) = m \cdot w_p\left(\frac{y}{m}\right) \quad (4.19)$$

Enfolding Eq. 4.19 into Eqs. 3.26-3.28, the final expressions for the compression recovery parameters are realized in terms of readily available measurements:

$$r(y) = \begin{cases} \sqrt{d \cdot \frac{m \cdot w_p(\frac{d}{m})}{2}} & : 0 \leq y \leq d \\ \sqrt{d \cdot \frac{m \cdot w_p(\frac{d}{m})}{2} + \frac{2d \cdot m [w_p(\frac{y}{m}) - w_p(\frac{d}{m})]}{\pi}} & : d \leq y \leq y_{center} \end{cases} \quad (4.20)$$

$$\gamma_x(y) = \begin{cases} \sqrt{\frac{d}{m \cdot w_p(\frac{d}{m})/2}} & : 0 \leq y \leq d \\ r(y) \cdot \frac{1}{m \cdot w_p(\frac{y}{m})/2} & : d \leq y \leq y_{center} \end{cases} \quad (4.21)$$

$$\gamma_z(y) = \begin{cases} \sqrt{\frac{m \cdot w_p(\frac{d}{m})/2}{d}} & : 0 \leq y \leq d \\ r(y) \cdot \frac{1}{d} & : d \leq y \leq y_{center} \end{cases} \quad (4.22)$$

where m is given by Eq. 4.18.

These parameters allow us to use the breast boundary on a mammogram and the compression depth to construct object curves in uncompressed space given the location of the source point and a point-of-interest on the image. The line-of-sight from image point to source point is depicted in Fig 4.3 along side the object curve that results from the application of $\gamma_x(y)$ and $\gamma_z(y)$. By determining the cross point with the corresponding object curve from with the mammogram's complementing view, it is possible to obtain realistic answers for the origin of a mammography-detected lesion. Now we put these parameters to use. The next section describes the implementation of the 3D localization parameters.

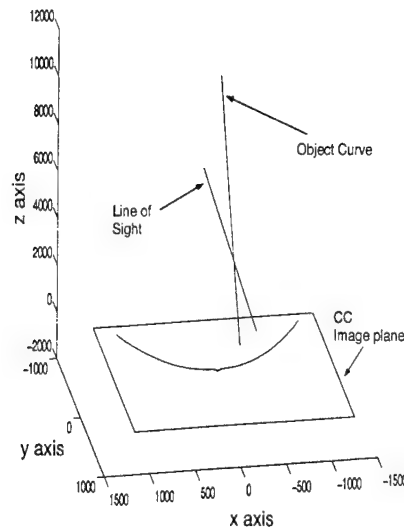


Figure 4.3 The object curve that results from the transformation of a line-of-sight from compressed space into uncompressed space.

4.4 3D Localization

This section establishes the algorithm in which a line-of-sight of a mammogram image point is transform to an object curve that represents potential 3D locations of the object in the uncompressed symmetrical breast. The 3D location of the object is found at the cross point of two object curves paired from the MLO and CC views.

4.4.1 Alignment and Reconstruction of Symmetric Breast. The goal of single-image alignment is to transform the two dimensional image axes $[i, j]$ into the three dimensional reference axes $[x, y, z]$ assigned in Section 3.2.2. The single-image transformation is necessary in order to calculate and apply the compression recovery parameters $\gamma_x(y)$ and $\gamma_y(x)$ properly. Additionally, the initial single-image alignment simplifies the secondary alignment that transforms the MLO reference axes and the CC reference axes to a common reference axes. This secondary view-to-horizontal alignment involves only a single rotation matrix operation.

4.4.1.1 Input Image Conventions. All angle and axis references discussed herein apply to the views of the left breast. Since the right breast's horizontal axis is a

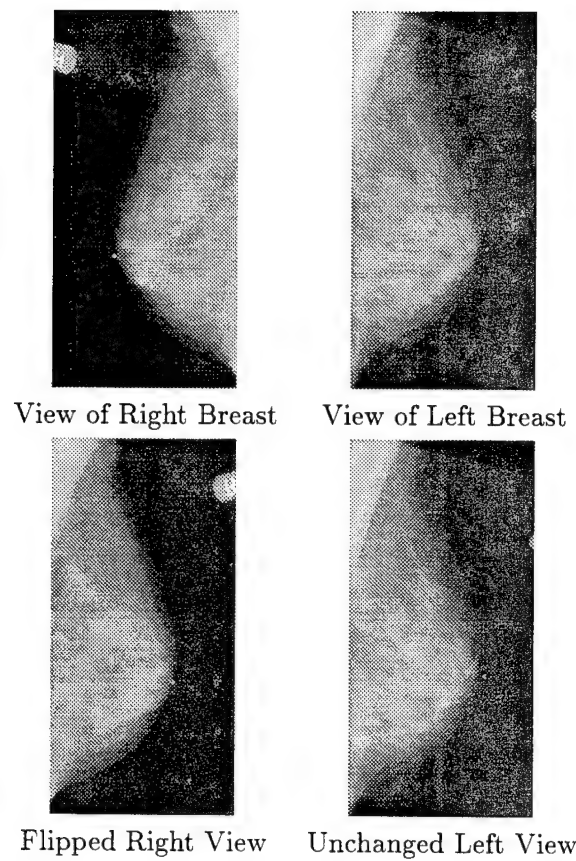


Figure 4.4 Input image convention: To simply processing algorithms, the left breast orientation was established as the standard orientation. Right breast images are flipped as shown.

mirror image of the left's, the image of the right breast is flipped to match the orientation of the image of the left breast as in Fig. 4.4. When processing is completed, a simple sign change to the horizontal axis is all that is required to reorient the three dimensional space of the right breast properly.

Conventions for the two dimensional image axes follow:

- The \hat{j} axis is perpendicular to the film edge against the chest wall. The positive \hat{j} axis runs from the posterior to the anterior breast regions.
- The \hat{i} axis is parallel to the film edge against the chest wall and runs positive from the lateral to the medial margins of the breast.

4.4.1.2 Initial Single-Image Alignment. For a given image, the locations of the origin and the reference axes are determined from the physical references of the imaged object: the aspect plane and the back-projections of the nipple line and y_{max} (the intersection of the nipple line with the breast boundary) as discussed in . Note that the source point is aligned to its fixed location above the film, so it is likely that the source point will not lie along the \hat{z} axis where $x = 0$ and $y = 0$.

The aspect plane is established as the $z = 0$ plane, and the image plane at the $z = -(d + pid)$ plane. At a height of $z = SID - (d + pid)$, the source point Q_i is positioned directly above the film edge oriented to the chest wall and midway between the adjacent film edges. The location of the origin $[0, 0, 0]^T$ is established at the back-projection of y_{max} into the aspect plane. As depicted in Fig. 4.5, the source point Q_i and any given image points P_i are translated in relation to the origin.

If the angle between the image axis \hat{j} and the nipple line is not zero, a rotation matrix is used to align given image points to \hat{y} . Clockwise rotation about the \hat{z} axis is achieved by [26]:

$$\mathbf{R}_z = \begin{bmatrix} \cos \theta & \sin \theta & 0 \\ -\sin \theta & \cos \theta & 0 \\ 0 & 0 & 1 \end{bmatrix} \quad (4.23)$$

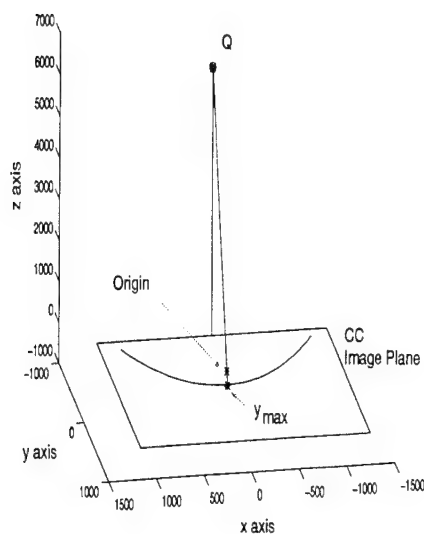


Figure 4.5 Initial single-image alignment for CC view: Translation of a CC mammogram so that axis of revolution is along \hat{y} axis and origin is at y_{pole} . $SID = 650mm$; $pid = 10mm$. The compression depth $2d$ is unknown so is assumed to be $45mm$, a typical compression depth.

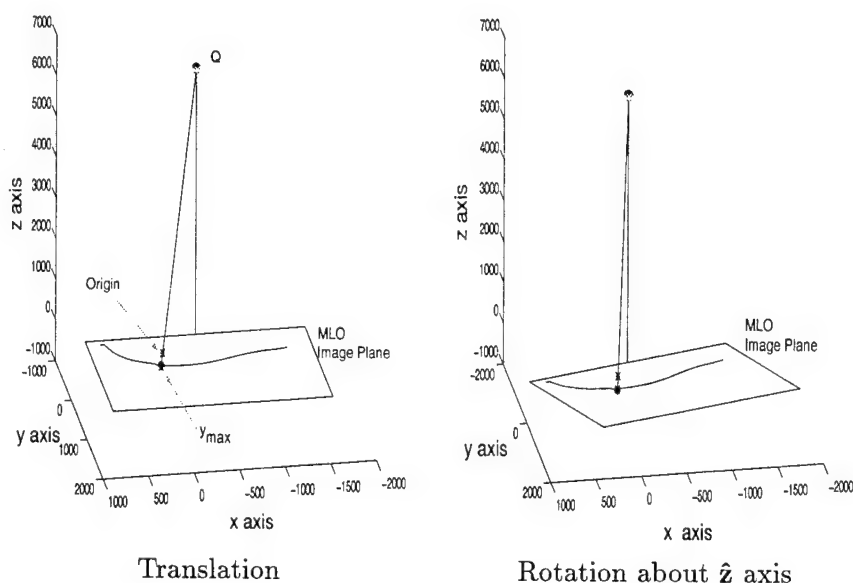


Figure 4.6 Initial single-image alignment for MLO view: Transformations required to place MLO image points in reference to the breast's axis of revolution. $SID = 650mm$; $pid = 10mm$. The compression depth is again assumed to be $45mm$.

so that image point P_i is transformed into point-of-interest P :

$$P = \mathbf{R}_z P_i \quad (4.24)$$

where

$$P = \begin{bmatrix} x_p \\ y_p \\ z_p \end{bmatrix} \quad (4.25)$$

and the source point is transformed in the same manner:

$$Q = \mathbf{R}_z Q_i \quad (4.26)$$

Angle θ is the angular difference between the \hat{j} image axis and the \hat{y} reference axis. In the medial lateral oblique view, θ is often negative with a magnitude of about 20° - 30° , and for the craniocaudal view, θ is usually 0 or a small positive angle. Figure 4.6 illustrates the orientation and rotation transformations required to place the image in reference to the breast's axis of revolution.

4.4.1.3 Compression Recovery. Given a point-of-interest P and its associated source point Q , the line-of-sight $L(t)$ in compressed space is calculated so that:

$$L(t) = P + \hat{\mathbf{v}}t \quad (4.27)$$

where

$$L(t) = \begin{bmatrix} x_L(t) \\ y_L(t) \\ z_L(t) \end{bmatrix} \quad (4.28)$$

and $\hat{\mathbf{v}}$ is a unit vector specifying the direction of source from the image point:

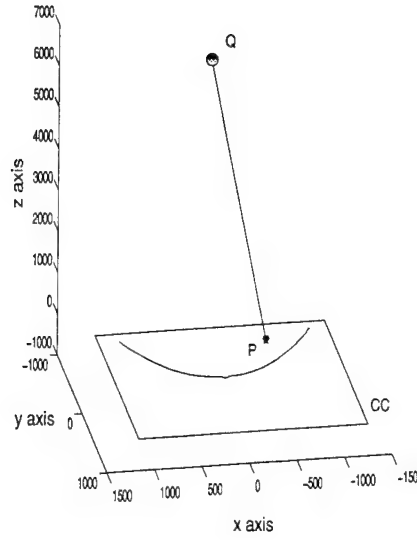


Figure 4.7 Line-of-Sight in compressed space.

$$\hat{\mathbf{v}} = \frac{\mathbf{Q} - \mathbf{P}}{|\mathbf{Q} - \mathbf{P}|} \quad (4.29)$$

where

$$\hat{\mathbf{v}} = \begin{bmatrix} v_x \\ v_y \\ v_z \end{bmatrix} \quad (4.30)$$

The result of the line-of-sight calculation is illustrated in Fig. 4.7. Recall that the line-of-sight $L(t)$ is affected by compression. Compression recovery is modeled by scaling $L(t)$ using $\mathbf{S}(y)$ from Eq. 3.29 with Eqs. 4.21-4.22. To express $L(t)$ in terms of y , we note that t is a weight to the unit vector $\hat{\mathbf{v}}$ so that the y component of $L(t)$ varies as $\frac{t}{v_y}$. Also, when $t = 0$, the $y_L = y_p$. Putting these two conditions together yields:

$$y = \frac{t}{v_y} + y_p \quad (4.31)$$

$$t = v_y \cdot (y - y_p) \quad (4.32)$$

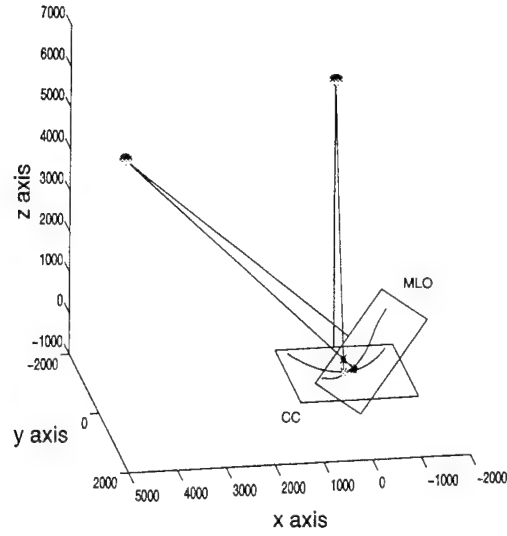


Figure 4.8 Orientation of MLO and CC views to the object horizontal. Angle β is unknown but assumed to be 45° .

and the expression for uncompressed object curve $L^U(y)$ (represented in Fig. 4.3) follows:

$$L^U(y) = \mathbf{S}(y) L(y) = \mathbf{S}(y) \cdot [P + \hat{\mathbf{v}} \cdot \mathbf{v}_y \cdot (y - y_p)] \quad (4.33)$$

4.4.1.4 View-to-Horizontal Transformation. The object curve is transformed to a common reference axes so the axes of each view are oriented properly to the horizontal of the object (See Fig. 4.8). This transformation involves a rotation about the $\hat{\mathbf{y}}$ axis. The rotation matrix for clockwise rotation about the $\hat{\mathbf{y}}$ axis is given as [26]:

$$\mathbf{R}_y = \begin{bmatrix} \cos \beta & 0 & -\sin \beta \\ 0 & 1 & 0 \\ \sin \beta & 0 & \cos \beta \end{bmatrix} \quad (4.34)$$

For the craniocaudal view, the angle $\beta = 0^\circ$ and this rotation transformation is not required. For the medial lateral view, the angle is typically 45° for the MLO view, but can range between 30° - 60° depending on the anatomy of the patient. Angle β must be recorded by the radiologic technologist to provide the best accuracy in processing.

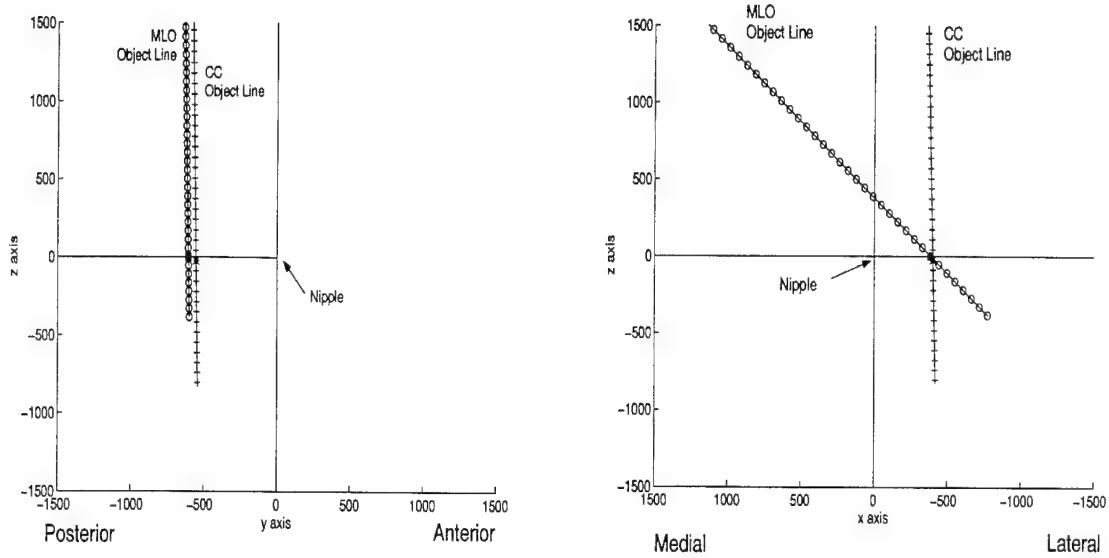


Figure 4.9 Discrete rendition of MLO and CC object lines. The nearest point from each line is used to narrow down the appropriate compression recovery matrix $\mathbf{S}(y)$ to be used in obtaining a more exact solution (see Fig. 4.10).

4.4.1.5 *Uncompressed Object Curve.* To summarize this section, the uncompressed object curve $L^H(y)$ as oriented to the object's horizontal is given by

$$L^H(y) = \mathbf{R}_y \mathbf{S}(y) L(y) = \mathbf{R}_y \mathbf{S}(y) \cdot [P + \hat{\mathbf{v}} \cdot v_y \cdot (y - y_p)] \quad (4.35)$$

This curve represents potential 3D locations of an object in the uncompressed symmetrical breast in reference to the horizontal axis.

4.4.2 *3D Localization.* Given corresponding points P_{cc} and P_{mlo} and their respective source points Q_{cc} and Q_{mlo} which have under gone the initial single-image alignment, the uncompressed object curves are given by:

$$L_{cc}^H(y_1) = \mathbf{R}_{y_{cc}} \mathbf{S}_{cc}(y_1) \cdot [P_{cc} + \hat{\mathbf{v}}_{cc} \cdot v_{cc_y} \cdot (y_1 - y_{cc_p})] \quad (4.36)$$

$$L_{mlo}^H(y_2) = \mathbf{R}_{y_{mlo}} \mathbf{S}_{mlo}(y_2) \cdot [P_{mlo} + \hat{\mathbf{v}}_{mlo} \cdot v_{mlo_y} \cdot (y_2 - y_{mlo_p})] \quad (4.37)$$

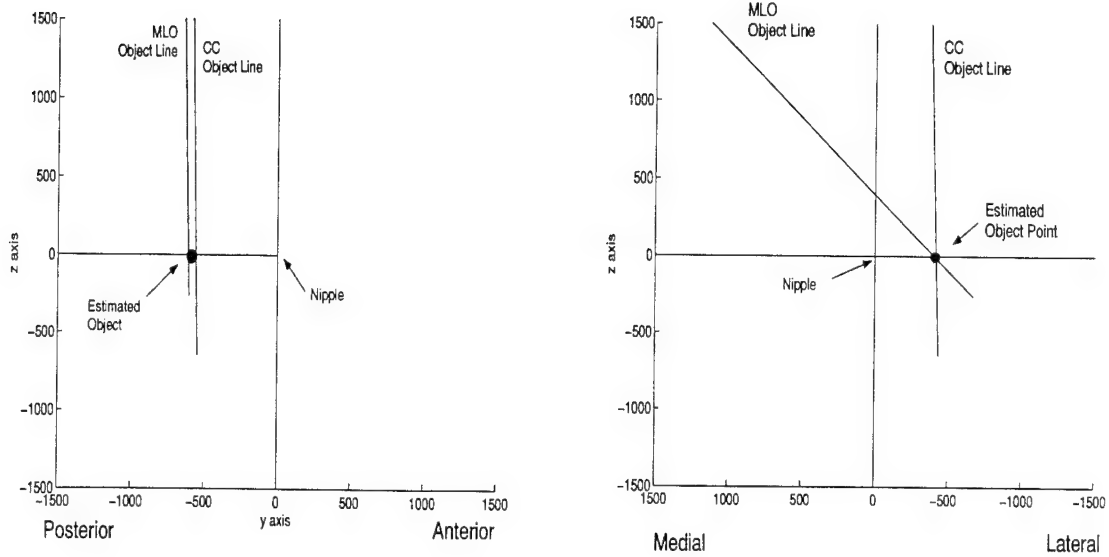


Figure 4.10 Lesion localized in three dimensions: Miss distance between MLO and CC solutions is $5mm$.

From the digitized mammogram, we have a discrete number of possible $S(y)$, usually less than 1000. Figure 4.9 details of the discrete points along both MLO and CC object curves. Iterating through the possible solutions to find the minimum distance between the curves is trivial with a computer. From sorting techniques, y_{1near} and y_{2near} are obtained from which the compression recovery matrix varies slowly as we approach the cross point. Using the lines given by,

$$L_{cc}^*(y_1) = \mathbf{R}_{y_{cc}} \mathbf{S}_{cc}(y_{1near}) \cdot [P_{cc} + \hat{\mathbf{v}}_{cc} \cdot v_{cc_y} \cdot (y_1 - y_{cc_p})] \quad (4.38)$$

$$L_{mlo}^*(y_2) = \mathbf{R}_{y_{mlo}} \mathbf{S}_{mlo}(y_{2near}) \cdot [P_{mlo} + \hat{\mathbf{v}}_{mlo} \cdot v_{mlo_y} \cdot (y_2 - y_{mlo_p})] \quad (4.39)$$

or

$$L_{cc}^*(y_1) = P_{cc}^* + \hat{\mathbf{v}}_{cc}^* \cdot v_{cc_y} \cdot (y_1 - y_{cc_p}) \quad (4.40)$$

$$L_{mlo}^*(y_2) = P_{mlo}^* + \hat{\mathbf{v}}_{mlo}^* \cdot v_{mlo_y} \cdot (y_2 - y_{mlo_p}) \quad (4.41)$$

it is possible to calculate the the nearest cross point and miss distance shown in Fig. 4.10 using the following algorithm [27]. Given

$$L_{cc}^*(t) = P_{cc}^* + \hat{\mathbf{v}}_{cc}^* t \quad (4.42)$$

$$L_{mlo}^*(s) = P_{mlo}^* + \hat{\mathbf{v}}_{mlo}^* s \quad (4.43)$$

where

$$t = v_{cc_y}(y_1 - y_{cc_p}) \quad (4.44)$$

$$s = v_{mlo_y}(y_2 - y_{mlo_p}) \quad (4.45)$$

Assume lines intersect, and find t_o where $L_{mlo}^*(t_o) = L_{cc}^*(t_o)$ so that:

$$P_{cc}^* + \hat{\mathbf{v}}_{cc}^* t_o = P_{mlo}^* + \hat{\mathbf{v}}_{mlo}^* t_o \quad (4.46)$$

Subtract point P_{cc}^* from both sides of Eq. 4.46, and cross multiply by vector $\hat{\mathbf{v}}_{mlo}^*$.

$$[\hat{\mathbf{v}}_{cc}^* \times \hat{\mathbf{v}}_{mlo}^*] t_o = [P_{mlo}^* - P_{cc}^*] \times \hat{\mathbf{v}}_{mlo}^* \quad (4.47)$$

To solve for t_o , one must solve the nested cross products which involves taking the determinate of the vectors $(P_{mlo}^* - P_{cc}^*)$, $\hat{\mathbf{v}}_{mlo}^*$, $\hat{\mathbf{v}}_{cc}^* \times \hat{\mathbf{v}}_{mlo}^*$:

$$t_o = \frac{Det[(P_{mlo}^* - P_{cc}^*), \hat{\mathbf{v}}_{mlo}^*, \hat{\mathbf{v}}_{cc}^* \times \hat{\mathbf{v}}_{mlo}^*]}{|\hat{\mathbf{v}}_{cc}^* \times \hat{\mathbf{v}}_{mlo}^*|^2} \quad (4.48)$$

Similarly,

$$s_o = \frac{Det[(P_{mlo}^* - P_{cc}^*), \hat{\mathbf{v}}_{cc}^*, \hat{\mathbf{v}}_{cc}^* \times \hat{\mathbf{v}}_{mlo}^*]}{|\hat{\mathbf{v}}_{cc}^* \times \hat{\mathbf{v}}_{mlo}^*|^2} \quad (4.49)$$

If $L_{cc}^*(t)$ and $L_{mlo}^*(s)$ intersect, the cross point \mathcal{O} is at $L_{cc}^*(t_o) = L_{mlo}^*(s_o)$. If the lines are skewed, the mean cross point \mathcal{O}_{mean} and the miss distance $\Delta\mathcal{O}$ are given by:

$$\mathcal{O}_{mean} = \frac{L_{cc}^*(t_o) + L_{mlo}^*(s_o)}{2} \quad (4.50)$$

$$\Delta\mathcal{O} = L_{cc}^*(t_o) - L_{mlo}^*(s_o) \quad (4.51)$$

The point \mathcal{O}_{mean} estimates the common object point in the uncompressed breast from which the points-of-interest P_{cc} and P_{mlo} were projected.

4.4.3 Cross Projection. If corresponding points-of-interest are unknown, a cross projection algorithm can be used to project a line-of-sight from one image onto the image plane of the other. The cross projected line of sight then may act as an indexing aid by narrowing down the location of a potential lesion. The following paragraphs work through the projection of a line of sight derived from P_{cc} , a point of interest from the craniocaudal view.

First, the uncompressed object curve of Eq. 4.35 is obtained and rotated into the reference axes of the opposing image:

$$L_{cc}^X(y) = \mathbf{R}_{y_{mlo}}^{-1} L_{cc}^H(y) = \mathbf{R}_{y_{mlo}}^{-1} \mathbf{R}_{y_{cc}} \mathbf{S}_{cc}(y) \cdot [P_{cc} + \hat{\mathbf{v}}_{cc} \cdot v_{cc_y} \cdot (y - y_{cc_p})] \quad (4.52)$$

$$\text{where} \quad (4.53)$$

$$L_{cc}^X(y) = \begin{bmatrix} x_{LX}(y) \\ y_{LX}(y) \\ z_{LX}(y) \end{bmatrix} \quad (4.54)$$

Next, to model the compression undergone by the imaged object in this aspect, the inverse of the compression recovery matrix $\mathbf{S}_{cc}(y_{LX})$ is applied to Eq. 4.52.

$$L_{cc}^{CX}(y) = \mathbf{S}_{cc}(y_{LX}) L_{cc}^X(y) \quad (4.55)$$

As the final step, the curve is the projected onto the image plane and transformed out of the MLO object reference axes into the original MLO image reference axes.

4.5 *Summary*

In this chapter, we have expressed the compression recovery parameters in measurable parameters and fit them into a 3D localization strategy. We are now ready to implement the 3D localization algorithms. The implementation is discussed in Chapter V.

V. Implementation

This chapter charts the 3D localization algorithm implementation describing how it fits into the architecture of a Computer Aided breast cancer Diagnosis system. The final section is a brief discussion of the modelling analysis of the algorithms.

5.1 Algorithm Implementation

5.1.1 Front End Processing. The natural place for the bulk of the 3D localization algorithms is in the Front End Processor of a CADx system. The primary responsibilities of the initial algorithm include collecting the breast features needed to perform initial single-image alignment discussed in Sections 4.4.1.2-4.4.1.4. Also, the algorithm can check the alignment using markers such as the BB in Fig. 2.6. The bread and butter of these algorithms is the ability to orient the source point to the film which thus demands preservation of film edge locations. The location of only three edges is required – the edge at the chest wall and its two adjacent edges – but if preserved in the images, the resulting data files would be cumbersome, and unnecessarily large for most CADx processing. Initial algorithms can subsample the image to navigate large images more readily. These front end algorithms determine the breast area and remove edges and view markers. Before cutting the image files down to a manageable, standardized size, the entire breast edge, the aspect parameters (β and y_{max}) and the locations of any nipple or lesion markers must be preserved to optimize 3D localization efforts. (For CADx systems that compare contralateral views, the outline of the pectoral muscle wall from contralateral MLO views will also provide a key reference [15].) A summary of the Front End Processor follows:

- Given imaging parameters:
 1. Fixed source-to-film location including the source-image distance SID
 2. Fixed podium-to-film distance, pid
 3. Variable rotation of the x-ray tube, angle β
 4. Variable compression depth, $2d$
- Locate \implies Evaluate:

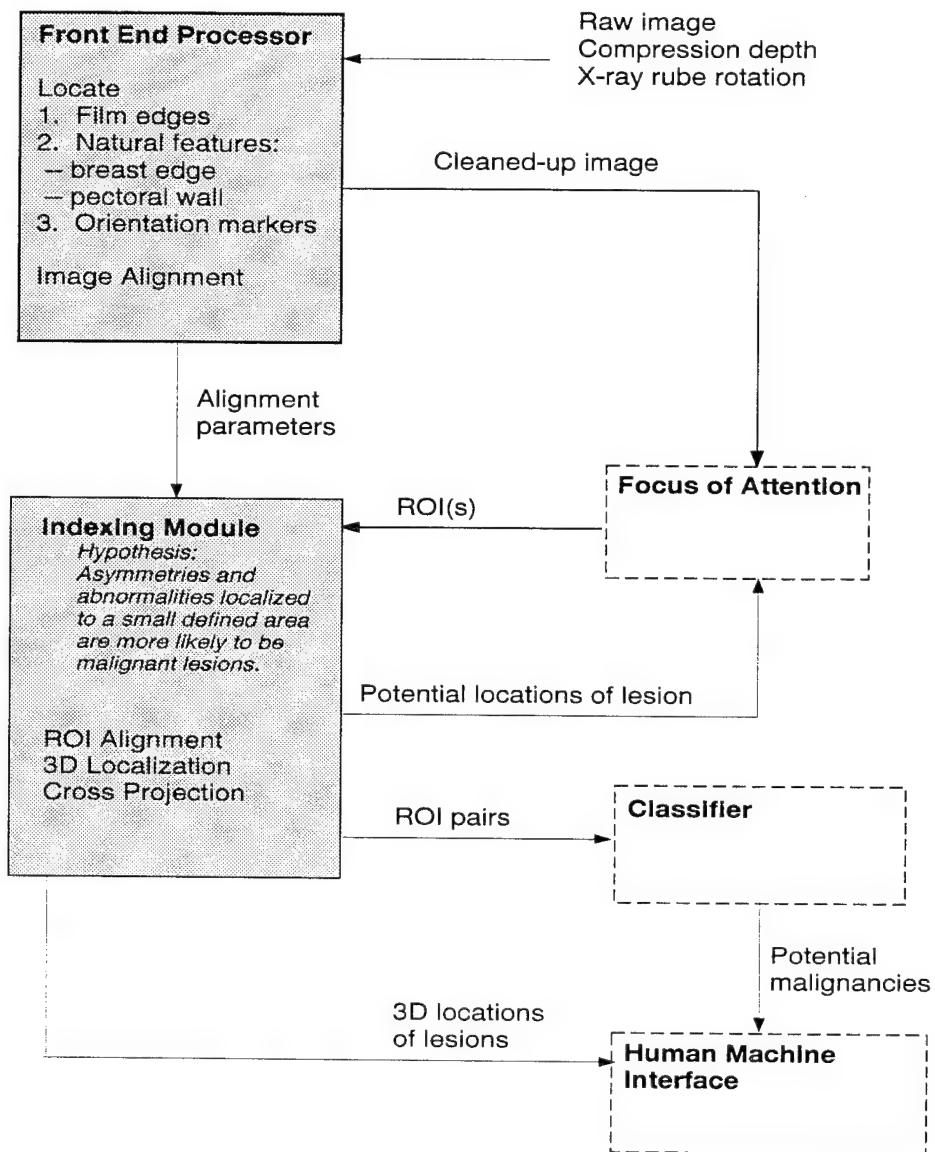


Figure 5.1 3D Algorithm Implementation within CADx System

1. Film edges \implies Source to image location
2. Breast boundary \implies Projected compressed object width, $w_p(y_p) \implies$ Compressed object width, $w(y)$
3. Angle θ between the nipple line and the \hat{j} image axis $\implies \hat{y}$ axis
4. Intersection of the nipple line and breast boundary, $y_{maz} \implies$ Origin reference point, y_{pole}

Results of the Front End Processor are passed to an Indexing module which will perform the actual 3D localizations on ROIs which the indexer receives from a Focus of Attention module.

5.1.2 Indexing. The Indexing module of a CADx system uses limiting hypotheses to sort out potential malignancies from list of regions of interest (ROIs) supplied by the system's sementor, the Focus of Attention module. The hypothesis checked by the 3D localizer is as follows: Asymmetries and abnormalities that can be verified by the complementing views of the breast and localized to a small 3D space are likely candidates for malignant regions.

The 3D localization algorithms convert the compressed space containing lines of sight from image ROIs to uncompressed space represented by object curves. The nearest cross points with object curves from the complementing image are evaluated to determine confidence in localization. Confidence factors will depend on miss distances of the object curves and the relative location of the 3D object point to the aspect plane and back-projected breast boundaries. ROI pairs that survive the 3D localization are passed to the classification module which categorizes lesions based on ROI features. The 3D location of potentially malignant regions are passed to the human machine interface for clinical use.

Additionally, object curve can be transformed in the compressed space of the complementing image and projected onto the image plane of this image providing expected locations of a lesion. Looser segmentation criteria in this area of the image may uncover the corresponding ROI without detrimentally affecting the false detection rate.

- Given \implies Evaluate:

1. ROI definition point \Rightarrow Line-of-sight in compressed space
 2. Line-of-sight in compressed space \Rightarrow Object curve in uncompressed space
 3. Object curves paired from complementing views \Rightarrow Nearest cross point and miss distance
- Additionally, Given \Rightarrow Evaluate:
 4. Object curve in uncompressed space \Rightarrow Same object curve transformed into the compressed space of the complementing view \Rightarrow Cross projection onto the complementing image
 5. Object curve or high confidence cross point \Rightarrow Comparable location in uncompressed space of the contralateral breast \Rightarrow Projections onto the contralateral views

Results of the Indexing module are passed to the Classification module which categorizes ROI pairs and the Human Machine Interface module which provides 3D locations of potential malignancies for clinical use. Additionally, expected lesion locations in a complementing view are passed to the Focus of Attention module.

5.2 *Implementation Modelling*

A mathematical model was created to evaluate the effectiveness of the algorithms and how uncertainties in measurement will affect alignment and results.

The model set up a simulated image: A 3D point was placed in a volume defined by a paraboloidal boundary. Uniform compression was applied to the volume and point. Using a real case source to film orientation, the compressed point and aspect-plane boundary of the compressed volume were projected onto an image plane.

From this simulated image, the algorithms for compression recovery and 3D localization were applied in an attempt to locate the original 3D point with degraded alignment parameters.

In modelled cases, errors in alignment parameters had the most significant effect on the y component of estimated object point. This is consistent with real data where miss

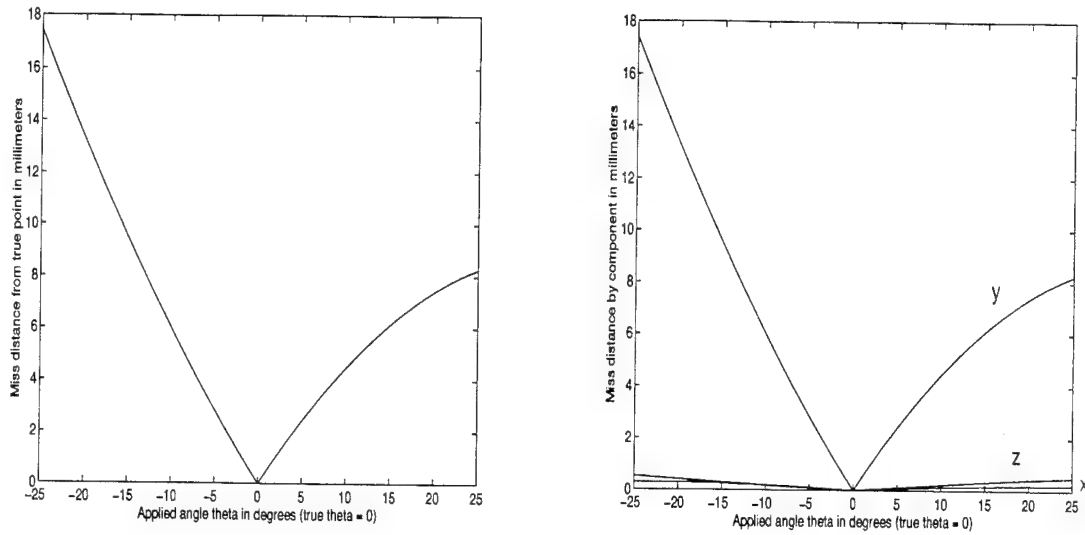


Figure 5.2 Modelled error dependency to angle θ , the angle between the nipple line and the image's \hat{j} axis.

distances between the nearest points from a MLO object curve and a CC object curve are generally greatest in the y direction. (See Fig. 4.10.)

Several runs were made using points far from the origin but within the volume of a typical breast. Result of a typical run is presented in Fig. 5.2. From these runs, the two most critical parameters of the alignment are the compression depth d and the angle θ between the nipple line and the image's \hat{j} axis.

By degrading all of alignment parameters at once, the overall sensitivity of the algorithms was gauged. In these runs, the miss distance from the true point could typically be held below 10 mm by keeping fixed parameter uncertainties to less than 1% and the measurable compression distance $2d$ to less than 10% of their true values. The rotation angles were kept within $\pm 5^\circ$. These numbers are relevant for a significant portion of the breast. However, tumors near the chest wall will be difficult to locate accurately as estimates of compression recovery parameters may prove insufficient.

VI. Conclusions

This thesis represents the first attempt to develop the components of a CADx system that would verify the detection of potentially malignant lesions through three dimensional localization. The 3D localization algorithms herein assume the use of a dedicated mammography unit that is equipped with a 90° compression paddle and that has fixed source-to-film orientation and podium-to-image distance.

The algorithms are developed specifically for standard mammography screenings where craniocaudal (CC) and medial lateral oblique (MLO) radiographic views are performed. Standard, properly performed patient positioning is necessary for quality images with landmarks that reflect the alignment and dimensions of the compressed breast.

Application of these algorithms requires the input of two additional imaging parameters: the rotation of the x-ray tube and the compression distance – distance between the compression plate and contact podium at the time of imaging. With these additional parameters, confidence in constructing object curves improves greatly.

This feasibility investigation located microcalcifications within 10-15 *mm* and eliminates quadrant ambiguities. Accuracy measures are based on knowing the fixed parameters, source-image distance and podium-image distance, of the mammography imaging system with accuracies of ± 5 *mm* and ± 2 *mm* respectively. The adjustable parameters, x-ray tube rotation angle and the distance from compression paddle to contact podium distance, are assumed to be known with accuracies of $\pm 5^\circ$ and ± 10 *mm* respectively. Accuracies of the adjustable parameters can be much better than this, and firm measurements will lead to much improved results.

Bibliography

1. J. W. Berg and R. V. P. Hutter, "Breast cancer," *Cancer, Supplement*, vol. 75, no. 1, pp. 257-269, 1995.
2. L. H. Baker, "Breast Cancer Detection Demonstration Project, 5 year summary report," *CA: a Cancer Journal for Clinicians*, vol. 32, pp. 194-225, 1982.
3. C. R. Smart, "Highlights of the evidence of benefit for women aged 40-49 years from the 14-year follow-up of the Breast Cancer Detection Demonstration Project," *Cancer: Supplement*, vol. 74, no. 1, pp. 296-300, 1994.
4. C. Byrne, C. R. Smart, K. C. Chu, and W. H. Hartmann, "Survival advantage differences by age: Evaluation of the extended follow-up of the Breast Cancer Detection Demonstration Project," *Cancer: Supplement*, vol. 74, no. 1, pp. 301-310, 1994.
5. L. W. Bassett and R. H. Gold, *Breast Cancer Detection: Mammography and Other Methods in Breast Cancer*. New York: Grune & Stratton, Inc., 2nd ed., 1987.
6. S. A. Feig, "Mammography screening of women aged 40-49 years: Benefit, risk, and cost considerations," *Cancer: Supplement*, vol. 76, no. 10, pp. 2097-2106, 1995.
7. F.-F. Yin, M. Giger, K. Doi, C. Metz, C. Vyborny, and R. Schmidt, "Computerized detection of mammographic masses in digital mammograms: Analysis of bilateral subtraction images," *Medical Physics*, vol. 18, no. 5, pp. 955-963, 1991.
8. C. M. Kocur, S. K. Rogers, L. Myers, T. Burns, J. Hoffmeister, J. Kenneth Bauer, and J. Steppe, "Neural network selection for breast cancer diagnosis." Accepted to IEEE Transactions on Medicine and Biology, to appear in early 1996, 1995.
9. H.-P. Chan, K. Doi, *et al.*, "Computer-aided detection and microcalcification in mammograms: Methodology and preliminary clinical study," *Investigative Radiology*, vol. 23, pp. 664-671, 1988.
10. Y. Chitre, A. P. Dhawan, and M. Moskowitz, "Artificial neural network based classification of mammographic microcalcifications using image structure features," *International Journal of Pattern Recognition and Artificial Intelligence*, vol. 7, no. 6, pp. 1377-1401, 1993.
11. J. Parker, D. R. Dance, *et al.*, "Classification of ductal carcinoma in situ by image analysis of calcifications from digital mammograms," *The British Journal of Radiology*, vol. 68, pp. 150-159, Feb. 1993.
12. J. W. Philip Kegelmeyer, "Evaluation of stellate lesion detection in a standard mammogram data set," *International Journal of Pattern Recognition and Artificial Intelligence*, vol. 7, pp. 1477-1492, Dec. 1993.
13. P. Miller and S. Astley, "Classification of breast tissue by texture analysis," *Image and Vision Computing*, vol. 10, no. 5, pp. 277-281, 1992.
14. D. Brett, G. McLeod, R. Oddy, G. Parkin, and A. Cowen, "Automatic microcalcification localization using matched fourier filtering," in *Digital Mammography*, (Amsterdam, The Netherlands), pp. 21-30, Elsevier Science B.V., 1994. 2nd International Workshop on Digital Mammography.

15. T.-K. Lau and W. Bischof, "Automated detection of breast tumors using the asymmetry approach," *Computer and Biomedical Research*, vol. 24, pp. 273-295, 1991.
16. W. Hand, J. Semmlow, L. Ackerman, and F. Alcorn, "Computer screening of xeromammograms: a technique for defining suspicious areas of the breast," *Computer and Biomedical Research*, vol. 12, pp. 445-460, 1979.
17. C. Kimme, B. O'Loughlin, and J. Sklansky, "Automatic detection of suspicious abnormalities in breast radiographs," in *Data Structures, Computer Graphics and Pattern Recognition*, pp. 427-447, New York: Academic Press, Inc., 1977.
18. W. Spiesberger, "Mammogram inspection by computer," *IEEE Transactions on Biomedical Engineering*, no. 4, pp. 213-219, 1979.
19. American College of Radiology, *Mammography Quality Control*, 1992.
20. S. Poteat. Interview with Resident Physicist for Radiology Programs at Wright Patterson Air Force Base Hospital, Aug. 1995.
21. A. Chisdak. Interview with Radiologic Technologist of Robert Packer Hospital, Feb. 1995.
22. G. James and R. C. James, *Mathematics Dictionary*. Princeton: D. Van Nostrand and Company, Inc., 3rd ed., 1968.
23. J. Bushberg, *The Essential Physics of Medical Imaging*. Baltimore: Williams & Wilkins, 1994.
24. S. L. Soo, *Particulates and Continuum: Multiphase Fluid Dynamics*. New York: Hemisphere Publishing Corporation, 1989.
25. A. Macovski, *Medical Imaging Systems*. Englewood Cliffs: Prentice-Hall, Inc., 1983.
26. R. C. Gonzalez and R. E. Woods, *Digital Image Processing*. New York: Addison-Wesley Publishing Company, Inc, 1992.
27. A. S. Glasser, ed., *Graphics Gems*. New York: Academic Press Professional, 1990.

Vita

Amy L. Magnus was born on 26 January 1967 in Morristown, New Jersey. Raised in Upstate New York, she graduated from Tioga Central High School in 1985. For her undergraduate work, she attended the Engineering College at the Rochester Institute of Technology from which she received a bachelors of science in electrical engineering in 1990. During her freshman year at college, she accepted a Reserve Officer Training Corps scholarship and, upon graduation, was commissioned into the Air Force.

On 16 January 1991 – one day before the Gulf War began – she entered active duty and began her service working for the Defense Support System (DSP) Space Program Office at Los Angeles Air Force Base, CA. Highlights of her first assignment included the launching of a DSP satellite, delivering the new system Multi Message Fusion to Space Command, and serving as Vice Chair for the 1994 Space and Missile Systems Center Engineering Competition.

In 1994 she was assigned to Wright-Patterson AFB to earn his masters of science degree in electrical engineering at the Air Force Institute of Technology. Following completion of the masters program, Capt Magnus entered the PhD program at AFIT.

Permanent address: 81 Guiles Road
Barton, New York 14534